

Nodal finite element approximation of peridynamics[†]

Prashant K. Jha^{a,*}, Patrick Diehl^{c,d}, Robert Lipton^{b,c}

^a*Department of Mechanical Engineering, South Dakota School of Mines and Technology, Rapid City, USA*

^b*Department of Mathematics, Louisiana State University, Baton Rouge, USA*

^c*Center for Computation and Technology, Louisiana State University, Baton Rouge, USA*

^d*Department of Physics and Astronomy, Louisiana State University, Baton Rouge, USA*

[†]**To appear in Computer Methods in Applied Mechanics and Engineering**

Abstract

This work considers the nodal finite element approximation of peridynamics, in which the nodal displacements satisfy the peridynamics equation at each mesh node. For the nonlinear bond-based peridynamics model, it is shown that, under the suitable assumptions on an exact solution, the discretized solution associated with the central-in-time and nodal finite element discretization converges to a solution in the L^2 norm at the rate $C_1\Delta t + C_2h^2/\epsilon^2$. Here, Δt , h , and ϵ are time step size, mesh size, and the size of the horizon or nonlocal length scale, respectively. Constants C_1 and C_2 are independent of h and Δt and depend on norms of the solution and nonlocal length scale. Several numerical examples involving pre-crack, void, and notch are considered, and the efficacy of the proposed nodal finite element discretization is analyzed.

Keywords: nonlocal fracture theory, peridynamics, cohesive dynamics, numerical analysis, finite element method

AMS Subject 34A34, 34B10, 74H55, 74S20

1. Introduction

Peridynamics is a reformulation of classical continuum mechanics introduced by Silling in [Silling \(2000\)](#); [Silling et al. \(2007\)](#). The strain inside the medium is expressed in terms of displacement differences as opposed to the displacement gradients, and the internal force at a material point is due to the sum of all pairwise interactions between a point and its neighboring points. The new formulation bypasses the difficulty incurred by displacement gradients and discontinuities, as in the case of classical fracture theories. The nonlocal fracture theory has been applied numerically to model the complex fracture phenomenon in materials, see, *e.g.*, [Weckner and Abeyaratne \(2005\)](#); [Silling and Bobaru \(2005\)](#); [Silling and Lehoucq \(2008\)](#); [Silling et al. \(2010\)](#); [Foster et al. \(2011\)](#); [Ha and Bobaru \(2010\)](#); [Agwai et al. \(2011\)](#); [Bobaru and Hu \(2012\)](#); [Ghajari et al. \(2014\)](#); [Lipton et al. \(2016\)](#); [Du et al. \(2018\)](#); [Lipton et al. \(2019\)](#); [Jha and Lipton \(2020b\)](#); [Jha et al. \(2021\)](#). [Diehl et al. \(2019\)](#) is referred for a comprehensive survey. In peridynamics, every point interacts with its neighbors inside a ball of fixed radius called the horizon. The size of the horizon sets the length scale of nonlocal interaction. When the forces between points are linear and when the nonlocal length scale tends to zero, it is seen that peridynamics converge to the classical linear elasticity, [Emmrich et al. \(2013\)](#); [Silling and Lehoucq \(2008\)](#); [Aksoylu and Unlu \(2014\)](#); [Mengesha and Du \(2015\)](#). For nonlinear forces, in which the bond behaves like an elastic spring for small strains and softens with increasing strains,

*Corresponding author (pjha.sci@gmail.com)

Email addresses: pjha.sci@gmail.com (Prashant K. Jha), pdiehl@cct.lsu.edu (Patrick Diehl), lipton@lsu.edu (Robert Lipton)

peridynamics converges in the small horizon limit to linear elastic fracture mechanics, where the material has a sharp crack, and away from a sharp crack the material is governed by linear elastodynamics, see Lipton (2016, 2014); Jha and Lipton (2020b, 2018b). For simulation of fracture using peridynamics, there are several choices, e.g., meshfree discretization Silling and Askari (2005); Trask et al. (2019) (see Seleson et al. (2016) for numerical convergence test and overview of existing meshfree methods for peridynamics), commonly used nodal-based discretization (similar to finite difference approximation of partial differential equations) Silling (2000, 2003); Silling and Lehoucq (2010); Jha and Lipton (2018a, 2019), and finite element approximations and their variants have been used in works such as Macek and Silling (2007); Madenci et al. (2018); Wildman et al. (2017); Chen and Gunzburger (2011); Diyaroglu et al. (2017); De Meo and Oterkus (2017); Anicode and Madenci (2022); Ni et al. (2018); Huang et al. (2019); Yang et al. (2019). To reduce the computational cost associated with the nonlocal interaction, coupled local (classical continuum mechanics) and peridynamics equations are also considered in which the local model is used away from cracking zone while the rest of the domain is modeled using peridynamics, see Liu and Hong (2012); Shoaiei et al. (2017).

Existing meshfree methods and methods similar to finite difference discretization where the nonlocal integral is approximated using the node-node interaction offer multiple advantages over standard finite element approximation of peridynamics, such as easy implementation and reduced computational cost. However, when compared to the finite element methods, meshfree methods suffer from poor numerical convergence, a lack of continuous representation of the displacement field, which could be crucial in post-processing, and difficulty in coupling peridynamics with other physics (e.g., heat equation and diffusion equation for corrosion).

Motivated by the above arguments, this work considers nodal finite element approximation (or, in brief, NFEA) that overcomes some of the limitations of the meshfree method while retaining the key features of finite element approximation, such as continuous representation of displacement, convergence estimates, and suitability for combining peridynamics with multiphysics models. In the nodal finite element approximation, the equation for the discretized displacement field is written at each mesh node. In contrast, in the standard finite element approximation (FEA) of peridynamics, the approximate solution satisfies the variational form of the peridynamics equation. Node-based calculations considered in this work are quite suitable for peridynamics/nonlocal equations, where a point nonlocally interacts with neighboring points at a distance larger than the mesh size. Classical finite element discretization of peridynamics, e.g., Jha and Lipton (2020a, 2021), involves computing interactions of a quadrature point with all neighboring quadrature points within a nonlocal neighborhood (typically a ball of radius greater than the mesh size). Thus, the computation cost is large and prohibitive if one chooses higher-order quadrature approximations. In contrast, the nodal finite element discretization considered in this work applies a discretized equation at each node, and nonlocal interactions are computed between the mesh nodes. Comparing the discretized equations in NFEA and FEA, NFEA includes the appearance of an additional error in representing the peridynamics force; see Section 3.2.

The main goal of this work is to perform an error analysis of the NFEA approximation and show a priori convergence of numerical solutions. The convergence of the numerical approximation is established by combining our previous work on a-priori convergence of finite element approximation of peridynamics Jha and Lipton (2021, 2020a) with new estimates that control the additional error introduced by nodal finite element approximation. For suitable initial conditions and boundary conditions, the NFEA solutions are shown to converge at a rate $C_1\Delta t + C_2h^2$, where Δt gives the size of the time step and h mesh size. Here, C_1 and C_2 are constants independent of Δt and h and depend on the nonlocal length scale ϵ , the norm of the exact solution, choice of influence function, and the peridynamics force potential (anti-derivative) ψ . Several fracture problems involving pre-crack, void, and notch are presented. These problems not only highlight the efficacy of the NFEA but also show the utility of peridynamics in nucleation and crack propagation.

The solution of the nonlocal problem is more regular than the local solution. For an evolution over the time interval $[0, t_F]$ a solution of the nonlocal problem is in $C^2[0, t_F]; H^2(D) \cap H_0^1(D)$, see Jha and Lipton (2021, 2020a). On the other hand the $\epsilon = 0$ limit solution with the limit taken with respect to the $C([0, t_F]; L^2(D))$ topology was shown to be in the space $C([0, t_F]; SBD(\Omega))$, see Lipton (2016). For a definition of $SBD(\Omega)$, see Ambrosio et al. (1997). The space of Special Functions of Bounded Deformation $SBD(\Omega)$ as well as $SBV(\Omega)$ is used to describe displacement fields in fractured media, see Ambrosio and Brades (1997). In this work, the location of the large strain represents the crack. The simulations show that

the regions of high strain are localized to thin regions of width on the order of the peridynamic horizon. The theoretical error bound deteriorates with the horizon, reflected in the growth of constants appearing in the a-priori error as the horizon becomes smaller. Motivated by these considerations, an alternate nodal interpolation given by the Clément interpolant is introduced. An improved a-priori convergence of nodal finite element approximation is proved. The implementation of Clément interpolations in NFEA and a-posteriori error estimates will be discussed in future work. It is seen that the nodal finite element approximation using Clément interpolation is asymptotically compatible under the assumption the L^∞ norm of the solution is bounded uniformly with respect to the horizon. This assumption is strongly supported in the simulations, [Section 7](#).

Outline of the article... In [Section 2](#), bond-based peridynamics theory is described, and the peridynamics equation of motion is presented. [Section 3](#) develops nodal finite element approximation, and it is compared with the standard finite element approximation. In [Section 4](#), a-priori convergence of an alternate nodal finite element approximation for the nonlinear bond-based model is stated and proved. In [Section 5](#), an a-priori convergence of the Clément nodal finite element approximation is proved. In [Section 6](#), the method is shown to be asymptotically compatible. Numerical experiments involving pre-crack, void, and notch are presented in [Section 7](#). Conclusions are drawn in [Section 8](#).

2. Bond-based peridynamics

Let $D \subset \mathbb{R}^d$, for $d = 2, 3$, be the material domain and $\epsilon > 0$ denote the size of the horizon. In the peridynamics formulation, a material point $\mathbf{x} \in D$ interacts with all the material points within a neighborhood of \mathbf{x} . Neighborhood of a point \mathbf{x} is taken to be the ball of radius ϵ centered at \mathbf{x} and is denoted by $H_\epsilon(\mathbf{x}) = \{\mathbf{y} \in \mathbb{R}^d : |\mathbf{y} - \mathbf{x}| < \epsilon\}$. In what follows, $\mathbf{x} \in D$ denote the material point, $\mathbf{u}(\mathbf{x}, t)$ the displacement of \mathbf{x} at time t for $t \in [0, t_F]$, and $\mathbf{z}(\mathbf{x}, t) = \mathbf{x} + \mathbf{u}(\mathbf{x}, t)$ current coordinate of \mathbf{x} . The bond strain (or bond stretch or pairwise strain) between material points \mathbf{x} and \mathbf{y} is defined as

$$\tilde{S}(\mathbf{y}, \mathbf{x}, t) = \frac{|\mathbf{z}(\mathbf{y}, t) - \mathbf{z}(\mathbf{x}, t)| - |\mathbf{y} - \mathbf{x}|}{|\mathbf{y} - \mathbf{x}|}. \quad (1)$$

For prototype microelastic brittle (PMB) material, the pairwise force between \mathbf{x} and \mathbf{y} takes the form (see [Silling \(2000\)](#); [Bobaru and Hu \(2012\)](#))

$$\tilde{\mathbf{f}}_{pmb}(\mathbf{y}, \mathbf{x}, t) = c J^\epsilon(|\mathbf{y} - \mathbf{x}|) \tilde{S}(\mathbf{y}, \mathbf{x}, t) \mu(\tilde{S}(\mathbf{y}, \mathbf{x}, t), t) \frac{\mathbf{z}(\mathbf{y}, t) - \mathbf{z}(\mathbf{x}, t)}{|\mathbf{z}(\mathbf{y}, t) - \mathbf{z}(\mathbf{x}, t)|}. \quad (2)$$

Here, c is a constant that depends on the elastic strength of a material, $J^\epsilon = J^\epsilon(|\mathbf{y} - \mathbf{x}|)$ the influence function, and $\mu(S, t)$ the bond-breaking function that models the breakage of the bond if the pairwise strain exceeds certain threshold strain:

$$\mu(\tilde{S}(\mathbf{y}, \mathbf{x}, t), t) = \begin{cases} 1, & \text{if } \tilde{S}(\mathbf{y}, \mathbf{x}, \tau) < S_c(\mathbf{y}, \mathbf{x}) \quad \forall \tau \leq t, \\ 0, & \text{otherwise.} \end{cases} \quad (3)$$

In the above, S_c is the critical bond strain between the material points \mathbf{y}, \mathbf{x} . In the PMB model, S_c is independent of \mathbf{y}, \mathbf{x} . In general, the value of the critical bond strain S_c depends on the critical fracture energy G_c and the elastic strength of the material. The total force at \mathbf{x} is given by the sum of the pairwise forces in the neighborhood of \mathbf{x} , *i.e.*,

$$\tilde{\mathbf{F}}_{pmb}(\mathbf{x}, t) = \int_{H_\epsilon(\mathbf{x}) \cap D} \tilde{\mathbf{f}}_{pmb}(\mathbf{y}, \mathbf{x}, t) d\mathbf{y}. \quad (4)$$

Under the small deformation assumption given by $|\mathbf{u}(\mathbf{x}) - \mathbf{u}(\mathbf{y})| \ll 1$, the bond strain $\tilde{S}(\mathbf{y}, \mathbf{x}, t)$ can be approximated by linearizing \tilde{S} as follows

$$S(\mathbf{y}, \mathbf{x}, t) = \frac{\mathbf{u}(\mathbf{y}, t) - \mathbf{u}(\mathbf{x}, t)}{|\mathbf{y} - \mathbf{x}|} \cdot \frac{\mathbf{y} - \mathbf{x}}{|\mathbf{y} - \mathbf{x}|} \approx \tilde{S}(\mathbf{y}, \mathbf{x}, t) \quad (5)$$

and the pairwise force taking the form

$$\mathbf{f}_{pmb}(\mathbf{y}, \mathbf{x}, t) = cJ^\epsilon(|\mathbf{y} - \mathbf{x}|)S(\mathbf{y}, \mathbf{x}, t)\mu(S(\mathbf{y}, \mathbf{x}, t), t)\frac{\mathbf{y} - \mathbf{x}}{|\mathbf{y} - \mathbf{x}|}, \quad (6)$$

where the force now acts along the bond vector in the reference configuration, *i.e.*, $\frac{\mathbf{y} - \mathbf{x}}{|\mathbf{y} - \mathbf{x}|}$. The total force at a material point is simply

$$\mathbf{F}_{pmb}(\mathbf{x}, t) = \int_{H_\epsilon(\mathbf{x}) \cap D} \mathbf{f}_{pmb}(\mathbf{y}, \mathbf{x}, t) d\mathbf{y}. \quad (7)$$

In this treatment, $\tilde{\cdot}$, *e.g.*, pairwise strain \tilde{S} and force $\tilde{\mathbf{F}}_{pmb}$, indicates the quantity associated with the large deformation, whereas the notations without $\tilde{\cdot}$, *e.g.*, S and \mathbf{F}_{pmb} , correspond to the small deformation assumption.

In the PMB model, the interaction between two material points comes to an abrupt stop as soon as the pairwise strain exceeds the critical strain. In contrast, pairwise force considered in Lipton (2016, 2014) regularizes the pairwise strain-force profile such that the bond under small strains behaves like a linear elastic material, and for larger strains, yields and softens with increasing strain, and eventually, the bond breaks for large strains. The force model introduced in Lipton (2016, 2014) is referred to as the regularized nonlinear peridynamics (RNP) material model. The pairwise potential – force given by the derivative of the potential – in the RNP model is defined by

$$\mathcal{W}^\epsilon(S(\mathbf{y}, \mathbf{x}, t)) = \frac{1}{w_d \epsilon^d} \omega(\mathbf{x}) \omega(\mathbf{y}) \frac{J^\epsilon(|\mathbf{y} - \mathbf{x}|)}{\epsilon |\mathbf{y} - \mathbf{x}|} \psi(|\mathbf{y} - \mathbf{x}| S(\mathbf{y}, \mathbf{x}, t)^2). \quad (8)$$

Here $w_d = |\{\mathbf{y} \in \mathbb{R}^d : |\mathbf{y}| < 1\}| = |H_1(\mathbf{0})|$ is the volume of a unit ball in the dimension d , *i.e.* $w_d = \pi$ in 2-d and $w_d = 4\pi/3$ in 3-d. $\omega : D \rightarrow [0, 1]$ is a boundary function which takes the value 1 for all $\mathbf{x} \in D_i := \{\mathbf{y} \in D : \text{dist}(\mathbf{y}, \partial D) > \epsilon\}$ and decays smoothly from 1 to 0 as \mathbf{x} approaches the boundary ∂D . The potential function $\psi : \mathbb{R}^+ \rightarrow \mathbb{R}$ is smooth, positive, and concave. For such a choice of ψ , the profile of potential \mathcal{W}^ϵ as a function of strain S is shown in Fig. 1. The pairwise force is written as (see Lipton (2016, 2014))

$$\begin{aligned} \mathbf{f}_{rnp}(\mathbf{y}, \mathbf{x}, t) &= 2 \partial_S \mathcal{W}^\epsilon(S(\mathbf{y}, \mathbf{x}, t)) \frac{\mathbf{y} - \mathbf{x}}{|\mathbf{y} - \mathbf{x}|} \\ &= \frac{4}{w_d \epsilon^d} \omega(\mathbf{x}) \omega(\mathbf{y}) \frac{J^\epsilon(|\mathbf{y} - \mathbf{x}|)}{\epsilon} \psi'(|\mathbf{y} - \mathbf{x}| S(\mathbf{y}, \mathbf{x}, t)^2) S(\mathbf{y}, \mathbf{x}, t) \frac{\mathbf{y} - \mathbf{x}}{|\mathbf{y} - \mathbf{x}|}. \end{aligned} \quad (9)$$

The critical strain S_c depends on the distance between material points \mathbf{y} and \mathbf{x} , and it is given by $S_c(\mathbf{y}, \mathbf{x}) = \pm r^*/\sqrt{|\mathbf{y} - \mathbf{x}|}$. $r^* > 0$ is the inflection point of function $r \mapsto \psi(r^2)$. The total force at \mathbf{x} is given by

$$\mathbf{F}_{rnp}(\mathbf{x}, t) = \int_{H_\epsilon(\mathbf{x}) \cap D} \mathbf{f}_{rnp}(\mathbf{y}, \mathbf{x}, t) d\mathbf{y}. \quad (10)$$

Fig. 2a and Fig. 2b shows PMB and RNP force profiles. The RNP model is amenable to a-priori convergence rate analysis and is investigated in this paper.

2.1. Peridynamics equation of motion using the RNP model

In the rest of the article, the pairwise strain S defined in (5) is considered, and the RNP model is employed where the pairwise force is given by (9). The peridynamics equation of motion for the displacement field $\mathbf{u} : D \times [0, t_F] \rightarrow \mathbb{R}^d$ is given by the Newton's second law as follows

$$\rho \partial_{tt}^2 \mathbf{u}(\mathbf{x}, t) = \mathbf{F}(\mathbf{u})(\mathbf{x}, t) + \mathbf{b}(\mathbf{x}, t), \quad (11)$$

where, ρ is the density, $\mathbf{F}(\mathbf{u})(\mathbf{x}, t)$ peridynamics force defined in (10), and $\mathbf{b}(\mathbf{x}, t)$ the body force per unit volume. Let ∂D be the boundary of the material domain D . For the analysis, the Dirichlet boundary condition is assumed, *i.e.*,

$$\mathbf{u}(\mathbf{x}, t) = 0, \quad \forall \mathbf{x} \in \partial D, \forall t \in [0, t_F]. \quad (12)$$

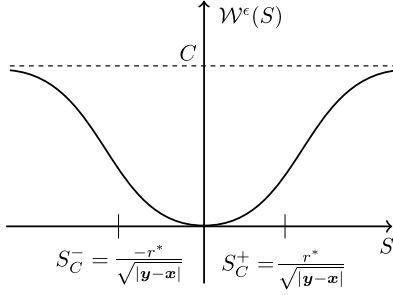


Figure 1: Profile of pairwise potential $\mathcal{W}^\epsilon(S)$ defined in (8). Here $C = \lim_{S \rightarrow \infty} \mathcal{W}^\epsilon(S)$.

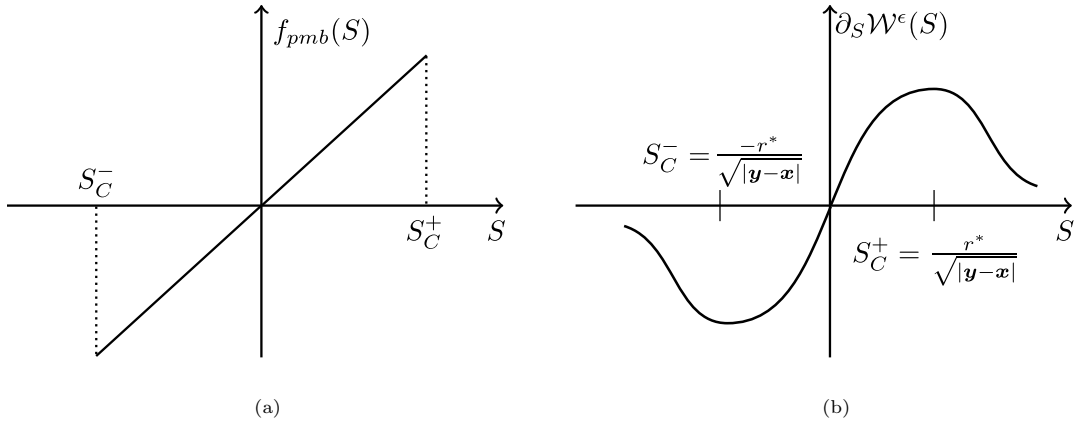


Figure 2: (a) Prototype microelastic brittle (PMB) material. Here, $f_{pmb}(S)$ is a scalar such that the bond force is $\mathbf{f}_{pmb}(\mathbf{y}, \mathbf{x}, t; \mathbf{u}) = f_{pmb}(S) \frac{\mathbf{y}-\mathbf{x}}{|\mathbf{y}-\mathbf{x}|}$; see (6). (b) Regularized nonlinear peridynamics (RNP) material.

The initial conditions for displacement and velocities are

$$\mathbf{u}(\mathbf{x}, 0) = \mathbf{u}_0(\mathbf{x}) \quad \text{and} \quad \partial_t \mathbf{u}(\mathbf{x}, 0) = \mathbf{v}_0(\mathbf{x}), \forall \mathbf{x} \in D. \quad (13)$$

In the rest of the article, density ρ is assumed to be constant.

For the RNP model, the initial boundary value problem given by (11) with (12) and (13) for $\mathbf{u}_0, \mathbf{v}_0 \in H^2(D) \cap H_0^1(D)$ and $\mathbf{b} \in C^2([0, t_F]; H^2(D) \cap H_0^1(D))$, is shown to be well-posed in the space $C^2([0, t_F]; H^2(D) \cap H_0^1(D))$; see (Jha and Lipton, 2021, Theorem 3.2). Here, $H_0^1(D)$ is given by the space of functions in $H^1(D)$ taking value zero on the boundary ∂D . In what follows, $\|\cdot\|$ and $\|\cdot\|_n$ will denote the $L^2(D)$ and $H^n(D)$ norms, for $n = 1, 2$, respectively.

3. Finite element approximation

Consider a discretization \mathcal{T}_h of the domain D by triangular (in 2-d) or tetrahedral (in 3-d) elements, where h denotes the size of mesh assuming that the elements are conforming and the mesh is shape regular. Let \bar{V}_h and V_h , with $V_h \subset \bar{V}_h$, denote the spaces of functions spanned by continuous piecewise linear interpolation over mesh \mathcal{T}_h such that $\bar{V}_h \subset H^1(D)$ and $V_h \subset H_0^1(D)$. It is further assumed that there exist constants $c_1, c_2 > 0$ such that

$$c_1 \sum_{i=1}^N |\mathbf{u}(\mathbf{x}_i)|^2 \leq \|\mathbf{u}\|^2 \leq c_2 \sum_{i=1}^N |\mathbf{u}(\mathbf{x}_i)|^2, \quad \forall \mathbf{u} \in \bar{V}_h, \quad (14)$$

where, N is the total number of mesh nodes, and \mathbf{x}_i is the material coordinate of i^{th} node.

For a continuous function \mathbf{u} on \bar{D} , it's continuous piecewise linear interpolant on \mathcal{T}_h is defined as

$$\mathcal{I}_h(\mathbf{u}) \Big|_T = \mathcal{I}_T(\mathbf{u}) \quad \forall T \in \mathcal{T}_h, \quad (15)$$

where, $\mathcal{I}_T(\mathbf{u})$ is the local interpolant associated with the finite element T such that

$$\mathcal{I}_T(\mathbf{u}) = \sum_{i \in N_T} \mathbf{u}(\mathbf{x}_i^T) \phi_i^T. \quad (16)$$

Here, N_T is the list of nodes as a vertex of the element T , \mathbf{x}_i^T the position of i^{th} vertex of the element T , and ϕ_i^T the linear interpolation function associated with the vertex i .

Application of Theorem 4.4.20 and Remark 4.4.27 in [Brenner and Scott \(2007\)](#) gives the bound on the interpolation error in L^2 norm as follows

$$\|\mathbf{u} - \mathcal{I}_h(\mathbf{u})\| \leq c_3 h^2 \|\mathbf{u}\|_2, \quad \forall \mathbf{u} \in H^2(D)^2 \quad (17)$$

and in L^∞ norm

$$\sup_{\mathbf{x}} |\mathbf{u}(\mathbf{x}) - \mathcal{I}_h(\mathbf{u})(\mathbf{x})| \leq c_4 h^2 \sup_{\mathbf{x} \in D} |\nabla^2 \mathbf{u}(\mathbf{x})|, \quad \forall \mathbf{u} \in C^2(D)^2. \quad (18)$$

Here, constants c_3, c_4 are independent of mesh size h .

Projection onto V_h . Let $\mathbf{r}_h(\mathbf{u})$ denote the projection of $\mathbf{u} \in H_0^1(D)$ on V_h with respect to the L^2 norm. It is defined by

$$\|\mathbf{u} - \mathbf{r}_h(\mathbf{u})\| = \inf_{\tilde{\mathbf{u}} \in V_h} \|\mathbf{u} - \tilde{\mathbf{u}}\| \quad (19)$$

and satisfies the orthogonality property

$$(\mathbf{r}_h(\mathbf{u}), \tilde{\mathbf{u}}) = (\mathbf{u}, \tilde{\mathbf{u}}), \quad \forall \tilde{\mathbf{u}} \in V_h. \quad (20)$$

Since $\mathcal{I}_h(\mathbf{u}) \in V_h$, from (17) it follows that

$$\|\mathbf{u} - \mathbf{r}_h(\mathbf{u})\| \leq \|\mathbf{u} - \mathcal{I}_h(\mathbf{u})\| \leq c_3 h^2 \|\mathbf{u}\|_2, \quad \forall \mathbf{u} \in H^2(D). \quad (21)$$

Clément interpolation. The Clément interpolant [Clément \(1975\)](#) is a linear operator $\mathcal{I}_h^C : L^2(\Omega)^2 \rightarrow V_h$ and to define it, let S_i denote the set of elements T with a common vertex i . Let $\mathcal{P}_1(S_i)$ be the space of continuous piecewise linear finite elements on S_i . Denote $P_i : L^2(S_i)^2 \rightarrow \mathcal{P}_1(S_i)$ as the L^2 -projection. Given $\mathbf{u} \in L^2(\Omega)^2$

$$\mathcal{I}_T^C(\mathbf{u}) = \sum_{i \in N_T} \mathcal{P}_i(\mathbf{u})(\mathbf{x}_i^T) \phi_i^T, \quad (22)$$

the bound on the interpolation error is

$$\|\mathbf{u} - \mathcal{I}_h^C(\mathbf{u})\|_t \leq Ch^{s-t} \|\mathbf{u}\|_s, \quad \forall \mathbf{u} \in H^s(D)^2, \quad (23)$$

for $0 \leq t \leq s \leq 2$ and $t \leq 1$, where $t = 0$ corresponds to the L^2 norm. Here, the constant C is independent of mesh size h . On writing $\mathcal{I}_h^C(\mathbf{u}) + \mathbf{u} - \mathbf{u}$ together with the triangle inequality delivers the stability

$$\|\mathcal{I}_h^C(\mathbf{u})\|_t \leq Ch^{s-t} \|\mathbf{u}\|_s, \quad \forall \mathbf{u} \in H^s(D)^2, \quad (24)$$

3.1. Nodal finite element approximation

Let Δt be the size of the time step and $t^k = k\Delta t$ be the time at step k . Let $\{\mathbf{U}_i^k\}_{1 \leq i \leq N}$ be the set of approximate nodal displacements at time step k . Associated to the discrete set $\{\mathbf{U}_i^k\}_{1 \leq i \leq N}$, displacement field $\mathbf{u}_h^k \in V_h$ can be defined as follows

$$\mathbf{u}_h^k(\mathbf{x}) \Big|_T = \sum_{i \in N_T} \mathbf{U}_i^k \phi_i(\mathbf{x}), \quad \mathbf{x} \in T, \quad \forall T \in \mathcal{T}_h. \quad (25)$$

The discrete solution satisfies, for all $1 \leq i \leq N$ and for $k \geq 1$,

$$\rho \frac{\mathbf{U}_i^{k+1} - 2\mathbf{U}_i^k + \mathbf{U}_i^{k-1}}{\Delta t^2} = \mathbf{F}(\mathbf{u}_h^k)(\mathbf{x}_i) + \mathbf{b}(\mathbf{x}_i, t^k) \quad (26)$$

and, for $k = 0$ (first time step),

$$\rho \frac{\mathbf{U}_i^1 - \mathbf{u}_0(\mathbf{x}_i)}{\Delta t^2} = \frac{1}{2} \mathbf{F}(\mathbf{u}_h^0)(\mathbf{x}_i) + \frac{1}{\Delta t} \mathbf{v}_0(\mathbf{x}_i) + \frac{1}{2} \mathbf{b}(\mathbf{x}_i, 0). \quad (27)$$

In the above, \mathbf{u}^0 and \mathbf{v}^0 are the initial conditions.

Fix $\mathbf{x} \in T$, where $T \in \mathcal{T}_h$. By multiplying interpolation function $\phi_i(\mathbf{x})$ to both sides of (26) and summing over $i \in N_T$, it follows that

$$\rho \frac{\mathbf{u}_h^{k+1}(\mathbf{x}) - 2\mathbf{u}_h^k(\mathbf{x}) + \mathbf{u}_h^{k-1}(\mathbf{x})}{\Delta t^2} \Big|_T = \sum_{i \in N_T} \mathbf{F}(\mathbf{u}_h^k)(\mathbf{x}_i) \phi_i(\mathbf{x}) + \sum_{i \in N_T} \mathbf{b}(\mathbf{x}_i, t^k) \phi_i(\mathbf{x}), \quad (28)$$

Let $\mathbf{F}_h(\mathbf{u}_h^k)$ and \mathbf{b}_h^k be the continuous piecewise linear interpolation of $\mathbf{F}(\mathbf{u}_h^k)$ and $\mathbf{b}(t^k)$, *i.e.*,

$$\begin{aligned} \mathbf{F}_h(\mathbf{u}_h^k)(\mathbf{x}) \Big|_T &= \sum_{i \in N_T} \mathbf{F}(\mathbf{u}_h^k)(\mathbf{x}_i) \phi_i(\mathbf{x}), \quad \mathbf{x} \in T, \quad \forall T \in \mathcal{T}_h, \\ \mathbf{b}_h^k(\mathbf{x}) \Big|_T &= \sum_{i \in N_T} \mathbf{b}(\mathbf{x}_i, t^k) \phi_i(\mathbf{x}), \quad \mathbf{x} \in T, \quad \forall T \in \mathcal{T}_h. \end{aligned}$$

Then, (28) can be written compactly as

$$\rho \frac{\mathbf{u}_h^{k+1} - 2\mathbf{u}_h^k + \mathbf{u}_h^{k-1}}{\Delta t^2} = \mathbf{F}_h(\mathbf{u}_h^k) + \mathbf{b}_h^k. \quad (29)$$

3.2. Comparison of NFEA with the standard FEA

Let $\hat{\mathbf{u}}_h^k \in V_h$ be the standard FEA solution that satisfies (see Jha and Lipton (2021)), for all test functions $\tilde{\mathbf{u}} \in V_h$ and $k \geq 1$,

$$\left(\rho \frac{\hat{\mathbf{u}}_h^{k+1} - 2\hat{\mathbf{u}}_h^k + \hat{\mathbf{u}}_h^{k-1}}{\Delta t^2}, \tilde{\mathbf{u}} \right) = (\mathbf{F}(\hat{\mathbf{u}}_h^k), \tilde{\mathbf{u}}) + (\mathbf{b}(t^k), \tilde{\mathbf{u}}). \quad (30)$$

To see the difference between the above discretization and the nodal FEA, multiply (29) with the test function $\tilde{\mathbf{u}} \in V_h$ and integrate over a domain D to have

$$\left(\rho \frac{\mathbf{u}_h^{k+1} - 2\mathbf{u}_h^k + \mathbf{u}_h^{k-1}}{\Delta t^2}, \tilde{\mathbf{u}} \right) = (\mathbf{F}_h(\mathbf{u}_h^k), \tilde{\mathbf{u}}) + (\mathbf{b}_h^k, \tilde{\mathbf{u}}). \quad (31)$$

Thus, in the NFEA, the exact peridynamics force \mathbf{F} and body force \mathbf{b} are replaced by their continuous piecewise linear interpolation \mathbf{F}_h and \mathbf{b}_h , respectively. By doing so, NFEA reduces the computational complexity of computing the integral of the product of peridynamics force and test function in (30) but at the cost of an additional discretization error; compare $(\mathbf{F}(\mathbf{u}_h^k), \tilde{\mathbf{u}})$ and $(\mathbf{b}^k, \tilde{\mathbf{u}})$ in (30) with $(\mathbf{F}_h(\mathbf{u}_h^k), \tilde{\mathbf{u}})$ and $(\mathbf{b}_h^k, \tilde{\mathbf{u}})$ in (29), respectively.

Next, a-priori convergence of NFEA solution \mathbf{u}_h^k to the exact solution $\mathbf{u}(t^k)$ in the limit mesh size, h , and time step, Δt , tending to zero is shown.

4. A-priori convergence of nodal FEA for nonlinear peridynamics models

This section establishes the convergence of the NFEA approximation to the exact peridynamics solution. The error analysis is focused on nonlinear peridynamics force (RNP), see (10), and exact solutions (displacement and velocity) are assumed to be $\mathbf{u}, \mathbf{v} \in C^2([0, t_F]; H^2(D) \cap H_0^1(D))$. Before the main result is presented, equations for errors are obtained, and the consistency of the numerical discretization is shown.

Equation (31) is equivalent to (29) and it can be decoupled into two equations by introducing $\mathbf{v}_h^k \in V_h$, \mathbf{v}_h^k being the approximate velocity field at time t^k , as follows

$$\begin{aligned} \left(\frac{\mathbf{u}_h^{k+1} - \mathbf{u}_h^k}{\Delta t}, \tilde{\mathbf{u}} \right) &= (\mathbf{v}_h^{k+1}, \tilde{\mathbf{u}}), & \forall \tilde{\mathbf{u}} \in V_h, \\ \left(\frac{\mathbf{v}_h^{k+1} - \mathbf{v}_h^k}{\Delta t}, \tilde{\mathbf{u}} \right) &= (\mathbf{F}_{rnp,h}(\mathbf{u}_h^k), \tilde{\mathbf{u}}) + (\mathbf{b}_h^k, \tilde{\mathbf{u}}), & \forall \tilde{\mathbf{u}} \in V_h. \end{aligned} \quad (32)$$

Similar to (Jha and Lipton, 2021, Section 5), L^2 projections of the exact displacement and velocity into V_h are compared with the approximate displacement and velocity, and the errors are defined as

$$\mathbf{e}_{u,h}^k = \mathbf{u}_h^k - \mathbf{r}_h(\mathbf{u}^k), \quad \mathbf{e}_{v,h}^k = \mathbf{v}_h^k - \mathbf{r}_h(\mathbf{v}^k),$$

where \mathbf{u}^k is the exact solution at time $t^k = k\Delta t$, $\mathbf{v}^k = \partial_t \mathbf{u}(t^k)$, and $\mathbf{r}_h(\mathbf{u}) \in V_h$ is the L^2 projection of \mathbf{u} defined in (19). Using the peridynamics equation of motion (11), (32), and property (20) of projection \mathbf{r}_h , it can be shown that

$$(\mathbf{e}_{u,h}^{k+1}, \tilde{\mathbf{u}}) = (\mathbf{e}_{u,h}^k, \tilde{\mathbf{u}}) + \Delta t(\mathbf{e}_{v,h}^{k+1}, \tilde{\mathbf{u}}) + \Delta t(\boldsymbol{\tau}_{u,h}^k, \tilde{\mathbf{u}}), \quad (33)$$

$$(\mathbf{e}_{v,h}^{k+1}, \tilde{\mathbf{u}}) = (\mathbf{e}_{v,h}^k, \tilde{\mathbf{u}}) + \Delta t(\mathbf{F}_{rnp}(\mathbf{u}^k) - \mathbf{F}_{rnp,h}(\mathbf{u}_h^k), \tilde{\mathbf{u}}) + \Delta t(\boldsymbol{\tau}_{v,h}^k, \tilde{\mathbf{u}}) + \Delta t(\mathbf{b}_h^k - \mathbf{b}(t^k), \tilde{\mathbf{u}}), \quad (34)$$

where, $\boldsymbol{\tau}_{u,h}^k, \boldsymbol{\tau}_{v,h}^k$ are consistency errors and take the form

$$\begin{aligned} \boldsymbol{\tau}_{u,h}^k &= \frac{\partial \mathbf{u}^{k+1}}{\partial t} - \frac{\mathbf{u}^{k+1} - \mathbf{u}^k}{\Delta t}, \\ \boldsymbol{\tau}_{v,h}^k &= \frac{\partial \mathbf{v}^k}{\partial t} - \frac{\mathbf{v}^{k+1} - \mathbf{v}^k}{\Delta t}. \end{aligned} \quad (35)$$

4.1. Key estimates

This section estimates the error terms in (33) and (34). In this direction, note that, if $\mathbf{u}, \mathbf{v} \in C^2([0, t_F]; H^2(D))$, then

$$\|\boldsymbol{\tau}_{u,h}^k\| + \|\boldsymbol{\tau}_{v,h}^k\| \leq C_t \Delta t, \quad C_t = \sup_t \|\partial_{tt}^2 \mathbf{u}(t)\| + \sup_t \|\partial_{ttt}^3 \mathbf{u}(t)\|. \quad (36)$$

Further, if $\mathbf{b} \in C([0, t_F]; H^2(D))$ then noting that \mathbf{b}_h^k is a linear interpolation of $\mathbf{b}(t^k)$ it can be easily shown using (17) that

$$\|\mathbf{b}_h^k - \mathbf{b}(t^k)\| \leq c_3 h^2 \sup_t \|\mathbf{b}(t)\|_2. \quad (37)$$

Focusing on the remaining consistency error term in (34), $\mathbf{F}_{rnp}(\mathbf{u}^k) - \mathbf{F}_{rnp,h}(\mathbf{u}_h^k)$, using the triangle inequality, the error can be shown to be bounded by the sum of the four terms as follows:

$$\begin{aligned} &\|\mathbf{F}_{rnp}(\mathbf{u}^k) - \mathbf{F}_{rnp,h}(\mathbf{u}_h^k)\| \\ &\leq \underbrace{\|\mathbf{F}_{rnp}(\mathbf{u}^k) - \mathbf{F}_{rnp,h}(\mathbf{u}^k)\|}_{=: I_1} + \underbrace{\|\mathbf{F}_{rnp,h}(\mathbf{u}^k) - \mathbf{F}_{rnp,h}(\mathcal{I}_h(\mathbf{u}^k))\|}_{=: I_2} \\ &\quad + \underbrace{\|\mathbf{F}_{rnp,h}(\mathcal{I}_h(\mathbf{u}^k)) - \mathbf{F}_{rnp,h}(\mathbf{r}_h(\mathbf{u}^k))\|}_{=: I_3} + \underbrace{\|\mathbf{F}_{rnp,h}(\mathbf{r}_h(\mathbf{u}^k)) - \mathbf{F}_{rnp,h}(\mathbf{u}_h^k)\|}_{=: I_4}. \end{aligned} \quad (38)$$

To bound the above terms, the following property of nonlinear peridynamics force \mathbf{F}_{rnp} is crucial.

Remark 4.1. Assuming that the domain D is a C^1 domain, the boundary function $\omega \in C^2(D)$, and the peridynamics potential ψ (see (8) or (9)) is smooth with up to 4th order bounded derivatives, from ([Jha and Lipton, 2021, Section 3](#)), it holds that

$$\|\mathbf{F}_{rnp}(\mathbf{u})\|_2 \leq \frac{L_2\|\mathbf{u}\|_2 + L_3\|\mathbf{u}\|_2^2}{\epsilon^{5/2}}, \quad \forall \mathbf{u} \in H^2(D). \quad (39)$$

Further, the peridynamics force satisfies the following Lipschitz continuity condition in the L^2 norm

$$\|\mathbf{F}_{rnp}(\mathbf{u}) - \mathbf{F}_{rnp}(\mathbf{v})\| \leq \frac{L_1}{\epsilon^2} \|\mathbf{u} - \mathbf{v}\| \quad \forall \mathbf{u}, \mathbf{v} \in L^2(D). \quad (40)$$

Here, constants L_1, L_2, L_3 are independent of \mathbf{u}, \mathbf{v} and depend on the influence function J and peridynamics force potential ψ . For future reference, L_1 , from ([Jha and Lipton, 2021, Section 3](#)), is given by

$$L_1 := 4 \underbrace{\left(\frac{1}{w_d} \int_{H_1(\mathbf{0})} \frac{J(|\xi|)}{|\xi|} d\xi \right)}_{=: \bar{J}_1} \underbrace{\left(\sup_r \left| \frac{d^2}{dr^2} \psi(r^2) \right| \right)}_{=: C_2} = 4\bar{J}_1 C_2. \quad (41)$$

The lemma below collects the bounds on the errors I_n , $n = 1, 2, 3, 4$.

Lemma 4.2. Consistency of the peridynamics force

For \mathbf{u}^k in $H^2(D) \cap C^2(D)$, the following estimates hold

$$\begin{aligned} I_1 &\leq \left[c_3 \frac{L_2\|\mathbf{u}^k\|_2 + L_3\|\mathbf{u}^k\|_2^2}{\epsilon^{5/2}} \right] h^2, & I_2 &\leq \left[\frac{L_1 c_4 \sqrt{\frac{c_2|D|}{c_1}}}{\epsilon^2} \sup_{\mathbf{x} \in D} |\nabla^2 \mathbf{u}^k(\mathbf{x})| \right] h^2, \\ I_3 &\leq \left[\frac{2c_3 L_1 \bar{n} \sqrt{\frac{c_2}{c_1}}}{\epsilon^2} \|\mathbf{u}^k\|_2 \right] h^2, & I_4 &\leq \left[\frac{L_1 \bar{n} \sqrt{\frac{c_2}{c_1}}}{\epsilon^2} \right] \|e_{u,h}^k\|. \end{aligned} \quad (42)$$

Here, c_i , $i = 1, 2, 3, 4$, are constants depending only on the triangulation T_h , see (17), (18), (14). Moreover, L_i , $i = 1, 2, 3$, are constants that only depend on the influence function J and the peridynamics force potential function ψ . Finally, the constant \bar{n} is given by

$$\bar{n} = \max_{T \in T_h} \{ \text{number of vertices of element } T \}. \quad (43)$$

Proof. Let us consider I_1 first. Since $\mathbf{u}^k \in H^2(D) \cap C^2(D)$, note that $\mathbf{F}_{rnp,h}(\mathbf{u}^k) = \mathcal{I}_h(\mathbf{F}_{rnp}(\mathbf{u}^k))$, where \mathcal{I}_h is the continuous piecewise linear interpolant. Using (17) and (39), it can be shown that

$$\begin{aligned} I_1 &= \|\mathbf{F}_{rnp}(\mathbf{u}^k) - \mathcal{I}_h(\mathbf{F}_{rnp}(\mathbf{u}^k))\| \leq c_3 h^2 \|\mathbf{F}_{rnp}(\mathbf{u}^k)\|_2 \\ &\leq \left[c_3 \frac{L_2\|\mathbf{u}^k\|_2 + L_3\|\mathbf{u}^k\|_2^2}{\epsilon^{5/2}} \right] h^2. \end{aligned}$$

Next, I_3 and I_4 are bounded from above. Let $\mathbf{w}_1, \mathbf{w}_2 \in V_h$, then both I_3 and I_4 are of the form $\|\mathbf{F}_{rnp,h}(\mathbf{w}_1) - \mathbf{F}_{rnp,h}(\mathbf{w}_2)\|$. Now, using the definition of \mathbf{F}_{rnp} in (10), it follows that

$$\begin{aligned} &\mathbf{F}_{rnp}(\mathbf{w}_1)(\mathbf{x}_i) - \mathbf{F}_{rnp}(\mathbf{w}_2)(\mathbf{x}_i) \\ &= \frac{4}{w_d \epsilon^{d+1}} \int_{H_\epsilon(\mathbf{x}) \cap D} \omega(\mathbf{x}_i) \omega(\mathbf{y}) J^\epsilon(|\mathbf{y} - \mathbf{x}_i|) \\ &\quad [\psi'(|\mathbf{y} - \mathbf{x}_i| S(\mathbf{y}, \mathbf{x}_i; \mathbf{w}_1)^2) S(\mathbf{y}, \mathbf{x}_i; \mathbf{w}_1) - \psi'(|\mathbf{y} - \mathbf{x}_i| S(\mathbf{y}, \mathbf{x}_i; \mathbf{w}_2)^2) S(\mathbf{y}, \mathbf{x}_i; \mathbf{w}_2)] \frac{\mathbf{y} - \mathbf{x}_i}{|\mathbf{y} - \mathbf{x}_i|} d\mathbf{y}. \end{aligned} \quad (44)$$

Let $\Psi(r) := \psi(r^2)$ then $\Psi'(r) = 2r\psi'(r^2)$ and $|\Psi'(r_1) - \Psi'(r_2)| \leq \sup_r |\Psi''(r)||r_1 - r_2|$. Since ψ is smooth and has up to 4 bounded derivatives, $\sup_r |\Psi''(r)| = \sup_r |\psi(r^2)| = C_2 < \infty$. Using the constant C_2 , it holds that

$$\begin{aligned} & 2|\psi'(|\mathbf{y} - \mathbf{x}_i|S(\mathbf{y}, \mathbf{x}_i; \mathbf{w}_1)^2)S(\mathbf{y}, \mathbf{x}_i; \mathbf{w}_1) - \psi'(|\mathbf{y} - \mathbf{x}_i|S(\mathbf{y}, \mathbf{x}_i; \mathbf{w}_2)^2)S(\mathbf{y}, \mathbf{x}_i; \mathbf{w}_2)| \\ & \leq C_2 \sqrt{|\mathbf{y} - \mathbf{x}_i|} |S(\mathbf{y}, \mathbf{x}_i; \mathbf{w}_1) - S(\mathbf{y}, \mathbf{x}_i; \mathbf{w}_2)| \\ & = C_2 \sqrt{|\mathbf{y} - \mathbf{x}_i|} \left| \frac{\mathbf{w}_1(\mathbf{y}) - \mathbf{w}_1(\mathbf{x}_i)}{|\mathbf{y} - \mathbf{x}_i|} \cdot \frac{\mathbf{y} - \mathbf{x}_i}{|\mathbf{y} - \mathbf{x}_i|} - \frac{\mathbf{w}_2(\mathbf{y}) - \mathbf{w}_2(\mathbf{x}_i)}{|\mathbf{y} - \mathbf{x}_i|} \cdot \frac{\mathbf{y} - \mathbf{x}_i}{|\mathbf{y} - \mathbf{x}_i|} \right| \\ & \leq C_2 \frac{|\mathbf{w}_1(\mathbf{y}) - \mathbf{w}_2(\mathbf{y})| + |\mathbf{w}_1(\mathbf{x}_i) - \mathbf{w}_2(\mathbf{x}_i)|}{\sqrt{|\mathbf{y} - \mathbf{x}_i|}}. \end{aligned}$$

Using the above bound and change in variable $\xi = (\mathbf{y} - \mathbf{x}_i)/\epsilon \in H_1(\mathbf{0})$, from (44), one can show that

$$\begin{aligned} & |\mathbf{F}_{rnp}(\mathbf{w}_1)(\mathbf{x}_i) - \mathbf{F}_{rnp}(\mathbf{w}_2)(\mathbf{x}_i)| \\ & \leq \frac{2C_2}{\epsilon^2 w_d} \int_{H_1(\mathbf{0})} \frac{J(|\xi|)}{\sqrt{|\xi|}} (|\mathbf{w}_1(\mathbf{x}_i + \epsilon\xi) - \mathbf{w}_2(\mathbf{x}_i + \epsilon\xi)| + |\mathbf{w}_1(\mathbf{x}_i) - \mathbf{w}_2(\mathbf{x}_i)|) d\xi \end{aligned} \quad (45)$$

and

$$\begin{aligned} & |\mathbf{F}_{rnp}(\mathbf{w}_1)(\mathbf{x}_i) - \mathbf{F}_{rnp}(\mathbf{w}_2)(\mathbf{x}_i)|^2 \\ & \leq 2 \left(\frac{2C_2}{\epsilon^2 w_d} \right)^2 \bar{J}_1 \int_{H_1(\mathbf{0})} \frac{J(|\xi|)}{|\xi|} (|\mathbf{w}_1(\mathbf{x}_i + \epsilon\xi) - \mathbf{w}_2(\mathbf{x}_i + \epsilon\xi)|^2 + |\mathbf{w}_1(\mathbf{x}_i) - \mathbf{w}_2(\mathbf{x}_i)|^2) d\xi, \end{aligned} \quad (46)$$

where, $\bar{J}_1 := \frac{1}{w_d} \int_{H_1(\mathbf{0})} J(|\xi|)/|\xi| d\xi$.

Next, using the property of the finite element function space V_h that relates L^2 norm to discrete l^2 norm in (14), it can be shown that

$$\begin{aligned} & \|\mathbf{F}_{rnp,h}(\mathbf{w}_1) - \mathbf{F}_{rnp,h}(\mathbf{w}_2)\|^2 \\ & \leq c_2 \sum_{i=1}^N |\mathbf{F}_{rnp}(\mathbf{w}_1)(\mathbf{x}_i) - \mathbf{F}_{rnp}(\mathbf{w}_2)(\mathbf{x}_i)|^2 \\ & \leq c_2 2 \left(\frac{2C_2}{\epsilon^2 w_d} \right)^2 \bar{J}_1 \int_{H_1(\mathbf{0})} \frac{J(|\xi|)}{|\xi|} \left[\sum_{i=1}^N (|\mathbf{w}_1(\mathbf{x}_i + \epsilon\xi) - \mathbf{w}_2(\mathbf{x}_i + \epsilon\xi)|^2 + |\mathbf{w}_1(\mathbf{x}_i) - \mathbf{w}_2(\mathbf{x}_i)|^2) \right] d\xi. \end{aligned} \quad (47)$$

Since $\mathbf{w}_1, \mathbf{w}_2 \in V_h$, using (14), it holds that

$$\sum_{i=1}^N |\mathbf{w}_1(\mathbf{x}_i) - \mathbf{w}_2(\mathbf{x}_i)|^2 \leq \frac{1}{c_1} \|\mathbf{w}_1 - \mathbf{w}_2\|^2. \quad (48)$$

Now, to estimate

$$\sum_{i=1}^N |\mathbf{w}_1(\mathbf{x}_i + \epsilon\xi) - \mathbf{w}_2(\mathbf{x}_i + \epsilon\xi)|^2,$$

consider any point $\mathbf{y} \in T$, where $T \in \mathcal{T}_h$. Denoting the set of vertices of an element T as N_T , it follows that

$$\begin{aligned} |\mathbf{w}_1(\mathbf{y}) - \mathbf{w}_2(\mathbf{y})|^2 &= \left| \sum_{i \in N_T} (\mathbf{w}_1(\mathbf{x}_i) - \mathbf{w}_2(\mathbf{x}_i)) \phi_i(\mathbf{y}) \right|^2 \\ &\leq |N_T| \sum_{i \in N_T} |\mathbf{w}_1(\mathbf{x}_i) - \mathbf{w}_2(\mathbf{x}_i)|^2 |\phi_i(\mathbf{y})|^2 \leq |N_T| \sum_{i \in N_T} |\mathbf{w}_1(\mathbf{x}_i) - \mathbf{w}_2(\mathbf{x}_i)|^2, \end{aligned}$$

where, in the above, the property of the interpolation function $\phi_i \leq 1$ is used, and $|N_T|$ gives the size of set N_T . Let $\bar{n} = \max_{T \in \mathcal{T}_h} |N_T|$, and define the map which returns the element T that contains the point \mathbf{y} by

$\Pi(\mathbf{y})$, i.e., $\Pi(\mathbf{y}) = T$ such that $\mathbf{y} \in \bar{T}$, $\bar{T} = T \cup \partial T$ is the closure of the set T . It is assumed that Π returns a unique element for all \mathbf{y} . Note that for \mathbf{y} on the boundary of an element T , \mathbf{y} could belong to more than one element. In such cases, Π is assumed to pick one element out of multiple elements randomly or through some selection scheme. It is easy to see now that

$$\sum_{i=1}^N |\mathbf{w}_1(\mathbf{x}_i + \epsilon\boldsymbol{\xi}) - \mathbf{w}_2(\mathbf{x}_i + \epsilon\boldsymbol{\xi})|^2 \leq \sum_{i=1}^N \left[\bar{n} \sum_{j \in N_{\Pi(\mathbf{x}_i + \epsilon\boldsymbol{\xi})}} |\mathbf{w}_1(\mathbf{x}_j) - \mathbf{w}_2(\mathbf{x}_j)|^2 \right].$$

In above double summation, each $|\mathbf{w}_1(\mathbf{x}_l) - \mathbf{w}_2(\mathbf{x}_l)|^2$ for $l = 1, \dots, N$ will be counted at max \bar{n} times, so

$$\begin{aligned} \sum_{i=1}^N |\mathbf{w}_1(\mathbf{x}_i + \epsilon\boldsymbol{\xi}) - \mathbf{w}_2(\mathbf{x}_i + \epsilon\boldsymbol{\xi})|^2 &\leq \sum_{i=1}^N \left[\bar{n} \sum_{j \in N_{\Pi(\mathbf{x}_i + \epsilon\boldsymbol{\xi})}} |\mathbf{w}_1(\mathbf{x}_j) - \mathbf{w}_2(\mathbf{x}_j)|^2 \right] \\ &\leq \bar{n}^2 \sum_{i=1}^N |\mathbf{w}_1(\mathbf{x}_i) - \mathbf{w}_2(\mathbf{x}_i)|^2. \end{aligned}$$

Combining the above inequality with (48), the following holds, for any $\boldsymbol{\xi} \in H_1(\mathbf{0})$,

$$\sum_{i=1}^N |\mathbf{w}_1(\mathbf{x}_i + \epsilon\boldsymbol{\xi}) - \mathbf{w}_2(\mathbf{x}_i + \epsilon\boldsymbol{\xi})|^2 \leq \frac{\bar{n}^2}{c_1} \|\mathbf{w}_1 - \mathbf{w}_2\|^2. \quad (49)$$

By combining (48) and (49) with (47), it can be shown that

$$\begin{aligned} &\|\mathbf{F}_{rnp,h}(\mathbf{w}_1) - \mathbf{F}_{rnp,h}(\mathbf{w}_2)\|^2 \\ &\leq 2c_2 \left(\frac{2C_2}{\epsilon^2 w_d} \right)^2 \frac{\bar{J}_1}{w_d} \int_{H_1(\mathbf{0})} \frac{J(|\boldsymbol{\xi}|)}{|\boldsymbol{\xi}|} \left[\frac{1 + \bar{n}^2}{c_1} \|\mathbf{w}_1 - \mathbf{w}_2\|^2 \right] d\boldsymbol{\xi} \\ &= \frac{(1 + \bar{n}^2)(c_2/c_1)8C_2^2 \bar{J}_1^2}{\epsilon^4} \|\mathbf{w}_1 - \mathbf{w}_2\|^2 \\ &\leq \left[\frac{\bar{n}\sqrt{c_2/c_1} L_1}{\epsilon^2} \|\mathbf{w}_1 - \mathbf{w}_2\| \right]^2, \end{aligned}$$

where, $L_1 = 4C_2 \bar{J}_1$ (see (41)). Using the above bound that holds for any $\mathbf{w}_1, \mathbf{w}_2 \in V_h$, one readily obtains

$$\begin{aligned} I_3 &= \|\mathbf{F}_{rnp,h}(\mathcal{I}_h(\mathbf{u}^k)) - \mathbf{F}_{rnp,h}(\mathbf{r}_h(\mathbf{u}^k))\| \leq \frac{\bar{n}\sqrt{c_2/c_1} L_1}{\epsilon^2} \|\mathcal{I}_h(\mathbf{u}^k) - \mathbf{r}_h(\mathbf{u}^k)\| \\ &\leq \frac{\bar{n}\sqrt{c_2/c_1} L_1}{\epsilon^2} [\|\mathcal{I}_h(\mathbf{u}^k) - \mathbf{u}^k\| + \|\mathbf{u}^k - \mathbf{r}_h(\mathbf{u}^k)\|] \leq \frac{\bar{n}\sqrt{c_2/c_1} L_1}{\epsilon^2} 2c_3 h^2 \|\mathbf{u}^k\|_2, \end{aligned} \quad (50)$$

where, (17) and (21) are utilized in the last step. Similarly, I_4 can be bounded from the above as follows

$$I_4 = \|\mathbf{F}_{rnp,h}(\mathbf{r}_h(\mathbf{u}^k)) - \mathbf{F}_{rnp,h}(\mathbf{u}_h^k)\| \leq \frac{\bar{n}\sqrt{c_2/c_1} L_1}{\epsilon^2} \|\mathbf{r}_h(\mathbf{u}^k) - \mathbf{u}_h^k\| = \frac{\bar{n}\sqrt{c_2/c_1} L_1}{\epsilon^2} \|\mathbf{e}_{u,h}^k\|, \quad (51)$$

where, the definition of the error $\mathbf{e}_{u,h}^k$ is used in the last step.

Next, I_2 is bounded from the above. Bounds established so far only used the fact that $\mathbf{u}^k \in H^2(D)$. However, to bound I_2 , additional regularity of $\mathbf{u}^k, \mathbf{u}^k \in H^2(D) \cap C^2(D)$, will be utilized.

$$\begin{aligned} I_2^2 &= \|\mathbf{F}_{rnp,h}(\mathbf{u}^k) - \mathbf{F}_{rnp,h}(\mathcal{I}_h(\mathbf{u}^k))\|^2 \leq 2c_2 \left(\frac{2C_2}{\epsilon^2 w_d} \right)^2 \frac{\bar{J}_1}{w_d} \\ &\int_{H_1(\mathbf{0})} \frac{J(|\boldsymbol{\xi}|)}{|\boldsymbol{\xi}|} \left[\sum_{i=1}^N (|\mathbf{u}^k(\mathbf{x}_i + \epsilon\boldsymbol{\xi}) - \mathcal{I}_h(\mathbf{u}^k)(\mathbf{x}_i + \epsilon\boldsymbol{\xi})|^2 + |\mathbf{u}^k(\mathbf{x}_i) - \mathcal{I}_h(\mathbf{u}^k)(\mathbf{x}_i)|^2) \right] d\boldsymbol{\xi}. \end{aligned} \quad (52)$$

Using the pointwise bound on the interpolant error, see (18), for $\mathbf{u}^k \in C^2(D)$, it follows

$$I_2^2 \leq c_2 2 \left(\frac{2C_2}{\epsilon^2 w_d} \right)^2 \frac{\bar{J}_1}{w_d} \int_{H_1(\mathbf{0})} \frac{J(|\xi|)}{|\xi|} \left[N c_4^2 h^4 \left(\sup_{\mathbf{x} \in D} |\nabla^2 \mathbf{u}^k(\mathbf{x})| \right)^2 \right] d\xi, \quad (53)$$

where recall that N is the number of mesh nodes. Consider $\bar{\mathbf{v}}_h = (\bar{v}_{1,h}, \bar{v}_{2,h}, \dots, \bar{v}_{d,h}) \in \bar{V}_h$, $d = 2, 3$ being the spatial dimension, such that $\bar{v}_{n,h} = 0$ for $n \geq 2$ and $\bar{v}_{1,h} = 1$. Then, from (14), it holds that

$$c_1 N \leq \|\bar{\mathbf{v}}_h\|^2 = |D| \quad \Rightarrow \quad N \leq \frac{|D|}{c_1}. \quad (54)$$

Using above in (53), it follows that

$$\begin{aligned} I_2^2 &\leq 2c_2 \frac{c_4^2 h^4 |D|}{c_1} \left(\sup_{\mathbf{y} \in D} |\nabla^2 \mathbf{u}^k(\mathbf{y})| \right)^2 \left(\frac{2C_2}{\epsilon^2 w_d} \right)^2 \frac{\bar{J}_1}{w_d} \int_{H_1(\mathbf{0})} \frac{J(|\xi|)}{|\xi|} d\xi \\ &\leq \left[\frac{2h^2 c_4 \sqrt{c_2 |D| / c_1} 2C_2 \bar{J}_1}{\epsilon^2} \sup_{\mathbf{x} \in D} |\nabla^2 \mathbf{u}^k(\mathbf{x})| \right]^2 \\ &\leq \left[\frac{h^2 L_1 c_4 \sqrt{c_2 |D| / c_1}}{\epsilon^2} \sup_{\mathbf{x} \in D} |\nabla^2 \mathbf{u}^k(\mathbf{x})| \right]^2, \end{aligned} \quad (55)$$

where the definition of L_1 is used in the last step. This completes the proof of lemma. \square

4.2. A-priori convergence

Let the discretization error E^k at the k^{th} step be given by

$$E^k = \|\mathbf{u}_h^k - \mathbf{u}(t^k)\| + \|\mathbf{v}_h^k - \mathbf{v}(t^k)\|. \quad (56)$$

Then, the application of triangle inequality and (21) gives

$$\begin{aligned} E^k &\leq \|\mathbf{u}_h^k - \mathbf{r}_h(\mathbf{u}(t^k))\| + \|\mathbf{v}_h^k - \mathbf{r}_h(\mathbf{v}(t^k))\| + \|\mathbf{r}_h(\mathbf{u}^k) - \mathbf{u}(t^k)\| + \|\mathbf{r}_h(\mathbf{v}^k) - \mathbf{v}(t^k)\| \\ &= \|\mathbf{e}_{u,h}^k\| + \|\mathbf{e}_{v,h}^k\| + C_p h^2, \end{aligned} \quad (57)$$

where

$$C_p = c_3 \left[\sup_t \|\mathbf{u}(t)\|_2 + \sup_t \|\partial_t \mathbf{u}(t)\|_2 \right]. \quad (58)$$

The main result is as follows.

Theorem 4.3. A-priori convergence of NFEA

If the solution $(\mathbf{u}, \mathbf{v} = \partial_t \mathbf{u})$ of the peridynamics equation (11) is such that $\mathbf{u}, \mathbf{v} \in C^2([0, t_F]; H^2(D) \cap H_0^1(D) \cap C^2(D))$ then the scheme is consistent and the total error E^k satisfies the following bound

$$\begin{aligned} &\sup_{k \leq t_F/\Delta t} E^k \\ &\leq C_p h^2 + \exp[t_F \frac{(1 + L_1 \bar{n} \sqrt{c_2/c_1}/\epsilon^2)}{1 - \Delta t}] \left[\|\mathbf{e}_{u,h}^0\| + \|\mathbf{e}_{v,h}^0\| + \left(\frac{t_F}{1 - \Delta t} \right) \left(C_t \Delta t + C_s \frac{h^2}{\epsilon^2} \right) \right], \end{aligned} \quad (59)$$

where, constants C_p and C_t are defined in (58) and (36), respectively, and the constant C_s is given by

$$\begin{aligned} C_s &= \left[\frac{c_3}{\epsilon^{5/2}} \left(L_2 \sup_t \|\mathbf{u}(t)\|_2 + L_3 (\sup_t \|\mathbf{u}(t)\|_2)^2 \right) \right] \\ &+ \left[\frac{L_1 c_4 \sqrt{\frac{c_2 |D|}{c_1}}}{\epsilon^2} \sup_t \sup_{\mathbf{x} \in D} |\nabla^2 \mathbf{u}(\mathbf{x}, t)| \right] + \left[\frac{2c_3 L_1 \bar{n} \sqrt{\frac{c_2}{c_1}}}{\epsilon^2} \sup_t \|\mathbf{u}(t)\|_2 \right]. \end{aligned} \quad (60)$$

The proof is similar to the proof of Theorem 5.1 in Jha and Lipton (2021) and relies on the estimates shown in Section 4.1.

5. An alternate nodal formulation based on the Clément interpolation

An improved a priori convergence result is observed when the Clément interpolant (see [Section 3](#)) is used in a nodal finite element formulation. More specifically, the Clément interpolation is used for the peridynamic force.

Let $\mathbf{F}_h^C(\mathbf{u}_h^k)$ be the Clément interpolation of $\mathbf{F}(\mathbf{u}_h^k)$, *i.e.*,

$$\mathbf{F}_h^C(\mathbf{u}_h^k)(\mathbf{x}) \Big|_T = \sum_{i \in N_T} \mathcal{P}_i(\mathbf{F}(\mathbf{u}_h^k))(\mathbf{x}_i) \phi_i(\mathbf{x}), \quad \mathbf{x} \in T, \quad \forall T \in \mathcal{T}_h, \quad (61)$$

where, recall from [Section 3](#) that $P_i : L^2(S_i)^2 \rightarrow \mathcal{P}_1(S_i)$ is the L^2 projection, S_i being the list of elements with i as the vertex and $\mathcal{P}_1(S_i)$ the space of continuous piecewise linear finite elements on S_i . Then, (28) is written as

$$\rho \frac{\mathbf{u}_h^{k+1} - 2\mathbf{u}_h^k + \mathbf{u}_h^{k-1}}{\Delta t^2} = \mathbf{F}_h^C(\mathbf{u}_h^k) + \mathbf{b}_h^k. \quad (62)$$

Previous analysis can be used to obtain the a-priori error estimates except for the peridynamics force. For the control of the error in peridynamics force, using the splitting of the error in (38), next results similar to [Theorem 4.2](#) are obtained bounding terms I_k , $k = 1, 2, 3, 4$.

First, an upper bound on I_2 is obtained. From (17), (40), (24), it follows that

$$\begin{aligned} I_2 &= \|\mathbf{F}_h^C(\mathbf{u}^k) - \mathbf{F}_h^C(\mathcal{I}_h(\mathbf{u}^k))\| = \|\mathcal{I}_h^C[\mathbf{F}(\mathbf{u}^k) - \mathbf{F}(\mathcal{I}_h(\mathbf{u}^k))]\| \\ &\leq C \|\mathbf{F}(\mathbf{u}^k) - \mathbf{F}(\mathcal{I}_h(\mathbf{u}^k))\| \leq \frac{CL_1}{\epsilon^2} \|\mathbf{u}^k - \mathcal{I}_h(\mathbf{u}^k)\| \\ &\leq \frac{c_3 CL_1 h^2}{\epsilon^2} \|\mathbf{u}^k\|_2. \end{aligned} \quad (63)$$

To bound I_3 , combining (17), (40), (24) to get

$$\begin{aligned} I_3 &= \|\mathbf{F}_h^C(\mathcal{I}_h(\mathbf{u}^k) - \mathbf{F}_h^C(r_h(\mathbf{u}^k)))\| = \|\mathcal{I}_h^C[\mathbf{F}(\mathcal{I}_h(\mathbf{u}^k) - \mathbf{F}(r_h(\mathbf{u}^k)))]\| \\ &\leq C \|\mathbf{F}(\mathcal{I}_h(\mathbf{u}^k) - \mathbf{F}(r_h(\mathbf{u}^k))\| \leq \frac{CL_1}{\epsilon^2} \|\mathcal{I}_h(\mathbf{u}^k) - r_h(\mathbf{u}^k)\| \\ &\leq \frac{CL_1}{\epsilon^2} \{ \|\mathcal{I}_h(\mathbf{u}^k) - \mathbf{u}^k\| + \|\mathbf{u}^k - r_h(\mathbf{u}^k)\| \} \leq 2 \frac{c_3 CL_1 h^2}{\epsilon^2} \|\mathbf{u}^k\|_2. \end{aligned} \quad (64)$$

Applying L^2 stability of the Clément interpolant and arguing as in (51) deliver

$$I_4 = \|\mathbf{F}_h^C(r_h(\mathbf{u}^k) - \mathbf{F}_h^C(\mathbf{u}_h^k))\| \leq \frac{\bar{n} \sqrt{c_2/c_1} L_1}{\epsilon^2} \|\mathbf{e}_{u,h}^k\|. \quad (65)$$

Lastly, term I_1 is bounded by applying (24) with $t = 0$ and $s = 2$ and (39) as follows

$$I_1 = \|\mathbf{F}(\mathbf{u}^k) - \mathbf{F}_h^C(\mathbf{u}^k)\| \leq Ch^2 \|\mathbf{F}(\mathbf{u}^k)\|_2 \leq \left[c_3 C \frac{L_2 \|\mathbf{u}^k\|_2 + L_3 \|\mathbf{u}^k\|_2^2}{\epsilon^{5/2}} \right] h^2. \quad (66)$$

Collecting the estimates (63), (64), (65), and (66) and arguing again as in the proof of Theorem 5.1 in [Jha and Lipton \(2021\)](#) gives

Theorem 5.1. *A-priori convergence of NFEA with Clément interpolation of peridynamics force*

If the solution $(\mathbf{u}, \mathbf{v} = \partial_t \mathbf{u})$ of the peridynamics equation (11) is such that $\mathbf{u}, \mathbf{v} \in C^2([0, t_F]; H^2(D) \cap H_0^1(D))$ then the scheme is consistent and the total error E^k satisfies the following bound

$$\begin{aligned} &\sup_{k \leq t_F/\Delta t} E^k \\ &\leq C_p h^2 + \exp[t_F \frac{(1 + L_1 \bar{n} \sqrt{c_2/c_1}/\epsilon^2)}{1 - \Delta t}] \left[\|\mathbf{e}_{u,h}^0\| + \|\mathbf{e}_{v,h}^0\| + \left(\frac{t_F}{1 - \Delta t} \right) \left(C_t \Delta t + C_s \frac{h^2}{\epsilon^2} \right) \right], \end{aligned} \quad (67)$$

where, constants C_p and C_t are defined in (58) and (36), respectively, and the constant C_s is given by

$$\begin{aligned} C_s = & \left[\frac{c_3}{\epsilon^{5/2}} \left(L_2 \sup_t \|\mathbf{u}(t)\|_2 + L_3 (\sup_t \|\mathbf{u}(t)\|_2)^2 \right) \right] \\ & + \left[\frac{3c_3 CL_1}{\epsilon^2} \sup_t \|\mathbf{u}(t)\|_2 \right]. \end{aligned} \quad (68)$$

This section is concluded with the following key remark.

Remark 5.2. The a-priori convergence rate for the alternate NFEA is an improvement over the rate given in Section [Theorem 4.3](#) as the constant C_s depends only on $\sup_t \|\mathbf{u}(t)\|_2$. However, it is more expensive to implement. Future work will investigate the efficiency of the alternate NFEA scheme. Additionally, the Clément interpolation will be used to design a-posteriori estimates for use in adaptive schemes for mesh refinement.

6. Asymptotic compatibility of Clément NFEA

In this section, the numerical error in initial values is assumed to be zero. The asymptotic compatibility is established using the $C([0, T], L^2(D))$ compactness of sequences of solutions to the RNP model associated with vanishing horizon together with the fact that the limit displacement \mathbf{u}^0 lies inside a dense subspace of $C([0, T], L^2(D))$.

To begin, write the peridynamic solution for the RNP model given in [Section 2](#) associated with horizon size ϵ as $\mathbf{u}^\epsilon(t)$. Motivated by simulations, see [Fig. 11](#) where the L^∞ norms of displacement are bounded for three different horizons, peridynamics solution is assumed to satisfy $\sup_{\epsilon > 0} \|\mathbf{u}^\epsilon\|_\infty < \infty$ for all ϵ . With this hypothesis, multiplying [Eq. \(11\)](#) by $\dot{\mathbf{u}}^\epsilon$, integrating by parts, and applying Grönwall's inequality to find as in [Lipton \(2016\)](#) that there is a sub-sequence denoted by \mathbf{u}^{ϵ_n} converging strongly to a limit function \mathbf{u}^0 in $C([0, t_F]; L^2(D))$, i.e.,

$$\lim_{n \rightarrow \infty} \max_{t \in [0, t_F]} \|\mathbf{u}^{\epsilon_n}(t) - \mathbf{u}^0(t)\|_{L^2(D)} = 0, \quad (69)$$

where, \mathbf{u}^0 belongs to SBD for every $t \in [0, t_F]$. Furthermore, there exists a constant C depending only on t_F bounding the Griffith (LEFM) energy,

$$\int_D \mu |\mathcal{E}\mathbf{u}^0(t)|^2 + \frac{\lambda}{2} |\operatorname{div} \mathbf{u}^0(t)|^2 dx + \mathcal{G}_c \mathcal{H}^{d-1}(J_{\mathbf{u}^0(t)}) \leq C, \quad d = 2, 3, \quad (70)$$

for $0 \leq t \leq t_F$, where, $J_{\mathbf{u}^0(t)}$ denotes the evolving fracture surface and $\mathcal{H}^{d-1}(J_{\mathbf{u}^0(t)})$ is its $d-1$ dimensional Hausdorff measure at time t . Here the shear moduli μ , and Láme moduli λ are given by explicit formulas expressed in terms of ψ' (derivative of the function ψ in the RNP force model), see [Lipton \(2016\)](#). An analogous observation for Hölder continuous solutions is made in [Jha and Lipton \(2018a\)](#).

Defining as before the discrete times $t^{k_n} = k\Delta t_n$, $k = 1, \dots, N$, where $N = t_F/\Delta t_n$, let the approximation of $\mathbf{u}^\epsilon(t^{k_n})$ based on the Clément NFEA is denoted by $(\mathbf{u}^\epsilon)_{h_n}^{k_n}$. Using the piecewise constant interpolation, the discrete solutions in times are extended to be defined at all times as follows:

$$(\mathbf{u}^\epsilon)_{h_n}^{k_n}(t) := (\mathbf{u}^\epsilon)_{h_n}^{k_n} \text{ for } t \text{ in the interval } ((k-1)\Delta t_n, k\Delta t_n). \quad (71)$$

Theorem 6.1. Asymptotic compatibility of NFEA with Clément interpolation of peridynamics force

Let $(\mathbf{u}^{\epsilon_n})_{h_n}^{k_n}$ be the Clément Nodal finite element approximation at time t^{k_n} to \mathbf{u}^{ϵ_n} , then there are sequences $\Delta t_n, h_n, \epsilon_n$, with $\Delta t_n \rightarrow 0$, $h_n \rightarrow 0$ and $\epsilon_n \rightarrow 0$ for $n = 1, 2, \dots$ such that

$$\lim_{n \rightarrow \infty} \max_{t \in [0, t_f]} \|(\mathbf{u}^{\epsilon_n})_{h_n}^{k_n}(t) - \mathbf{u}^0(t)\|_{L^2(D)} = 0.$$

Remark 6.2. It is noted that the method is not uniformly convergent with horizon ϵ_n as the constants multiplying the ratio $\frac{h_n^2}{\epsilon_n^2}$ go to ∞ as $\epsilon_n \rightarrow 0$.

To establish [Theorem 6.1](#), define

$$\tilde{\mathbf{u}}^{\epsilon_n, k_n}(t) := \mathbf{u}^{\epsilon_n}(t^{k_n}) \text{ for } t \text{ in the interval } ((k-1)\Delta t_n, k\Delta t_n), \quad (72)$$

and apply the triangle inequality

$$\begin{aligned} \max_{t \in [0, t_f]} \|(\mathbf{u}^{\epsilon_n})_{h_n}^{k_n}(t) - \mathbf{u}^0(t)\|_{L^2(D)} &\leq \max_{t \in [0, t_f]} \|(\mathbf{u}^{\epsilon_n})_{h_n}^{k_n}(t) - \tilde{\mathbf{u}}^{\epsilon_n, k_n}(t)\|_{L^2(D)} + \max_{t \in [0, t_f]} \|\tilde{\mathbf{u}}^{\epsilon_n, k_n}(t) - \mathbf{u}^{\epsilon_n}(t)\|_{L^2(D)} \\ &+ \max_{t \in [0, t_f]} \|\mathbf{u}^{\epsilon_n}(t) - \mathbf{u}^0(t)\|_{L^2(D)} := A_1 + A_2 + A_3. \end{aligned} \quad (73)$$

From [Theorem 5.1](#)

$$A_1 \leq \max_{t^{k_n}} \|(\mathbf{u}^{\epsilon_n})_{h_n}^{k_n} - \mathbf{u}^{\epsilon_n}(t^{k_n})\|_{L^2(D)} \leq \frac{C^{\epsilon_n}}{\epsilon_n^2} (C_t \Delta t_n + C_s h_n^2), \quad (74)$$

where, $C^{\epsilon_n} \rightarrow \infty$ as $\epsilon_n \rightarrow 0$. Set $O_{k_n} = ((k-1)\Delta t_n, k\Delta t_n)$, and from [Theorem 2.3 of Lipton \(2016\)](#) one has

$$A_2 \leq \max_{k_n} \max_{t \in O_{k_n}} \|\mathbf{u}^{\epsilon_n}(t^{k_n}) - \mathbf{u}^{\epsilon_n}(t)\|_{L^2(D)} \leq C \Delta t_n, \quad (75)$$

where, the constant C is independent of ϵ_n , \mathbf{u}^{ϵ_n} and Δt_n . From the strong convergence [Eq. \(69\)](#), it is clear A_3 converges to 0 for $\epsilon_n \rightarrow 0$. Thus, given a tolerance $\tau > 0$, ϵ_n can be selected to be sufficiently small so that $A_3 < \tau/3$. From [Eq. \(75\)](#), the size of time steps Δt_n can be chosen sufficiently small so that $A_2 \leq \tau/3$. Lastly, given ϵ_n from [Eq. \(74\)](#), mesh size h_n and Δt_n can be selected sufficiently small to have $A_1 \leq \tau/3$, and combining $A_1 + A_2 + A_3 < \tau$ proving the theorem.

7. Numerical results

This section presents results involving fracture evolution under different loading conditions and geometries. First, the procedure to numerically compute the peridynamics force is detailed, and the implementation of the NFEA method is briefly presented. In the implementation, integration over a horizon in the nodal peridynamics force is approximated by discrete summation involving node-node interaction; this is similar to the commonly used meshfree method and allows the NFEA method to be computationally efficient. Next, the material properties for numerical examples and calibration of the parameters in the peridynamics constitutive law are detailed. The remaining subsections are devoted to the numerical results. The first example concerns a simple non-fracture problem involving a square domain subjected to displacement-controlled loading, and the mesh convergence of the NFEA method is analyzed. The results show convergence rates depend on the two meshes used in the rate calculation, and the rates are close to or above 1.75. In the second example, a Mode-I crack propagation problem is taken up. Using this example, several results are obtained: first, the convergence rate with mesh refinement; second, the solution is compared with the solution from the meshfree discretization based on [Silling and Askari \(2005\)](#); [Lipton et al. \(2019\)](#); [Jha and Lipton \(2019\)](#); and, third, the localization of damage zone is shown with refinement of horizon. The third example involves a square specimen with a circular hole under displacement-controlled axial loading. This example shows the nucleation of the crack from the two points in the boundary of a hole. The fourth example is about the bending loading of the V-notch structure. This example also shows the crack nucleation. The last problem motivated by ([Dai et al., 2015](#), Figure 18) includes a rectangle specimen with a hole and pre-crack. This example shows the effect of stress concentration near the hole on crack path and propagation. The section ends with a discussion of the crack speeds for the four problems.

Numerical results were obtained using a code similar to the C++ code NLMech [Diehl et al. \(2020\)](#); [Jha and Diehl \(2021\)](#). In all results, the mesh consisted of linear triangle elements. The second-order quadrature scheme calculates the integration over a finite element (triangle elements); see next subsection. The strain field – symmetric gradient of the displacement – is constant over each element and computed at the element's center. For the triangulation of a domain with a void and notch, an open-source library Gmsh [Geuzaine and Remacle \(2009\)](#) is utilized, and Paraview [Ahrens et al. \(2005\)](#) is used to visualize the results.

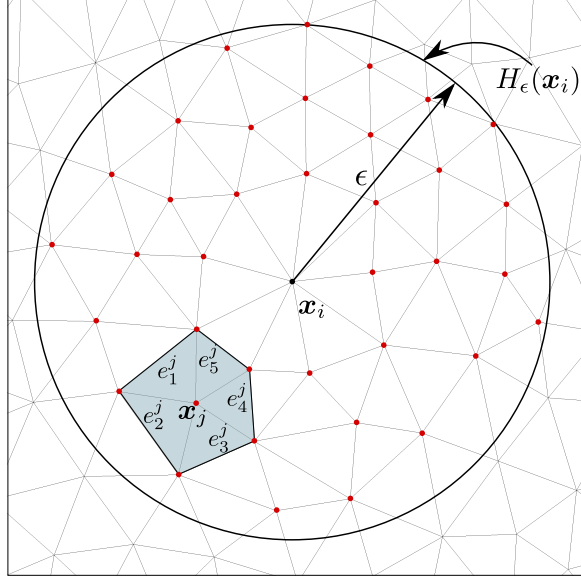


Figure 3: Typical mesh node \mathbf{x}_i and one of the neighboring nodes \mathbf{x}_j in an example 2-d finite element mesh. All the red nodes contribute to the force at \mathbf{x}_i . The set $E_j = \{e_k^j\}_{k=1}^5$ of elements with the node \mathbf{x}_j as the vertex is shown in grey.

7.1. Computation of a peridynamics force in NFEA

This section develops a computationally efficient approximation of the peridynamics forces at nodes based on the discrete summation of the node-node interaction. As a result of the approximation, the NFEA and meshfree methods will have the same computational complexity. The downside of the approximation, however, is the loss of accuracy. In the a-priori error analysis, the discretization error of nodal peridynamics forces is not considered.

Let $\mathbf{u}_h^k, \mathbf{v}_h^k \in V_h$ be the finite element displacement and velocity functions, V_h being the finite element space (see (25) and Section 3.1). Corresponding to \mathbf{u}_h^k and \mathbf{v}_h^K , suppose $\mathbf{U}^k, \mathbf{V}^k$ are nodal displacement and velocity vectors, respectively, i.e., $\mathbf{U}^k = (\mathbf{U}_1^k, \dots, \mathbf{U}_N^k), \mathbf{V}^k = (\mathbf{V}_1^k, \dots, \mathbf{V}_N^k)$. Velocity is given by

$$\mathbf{V}_i^k = (\mathbf{U}_i^k - \mathbf{U}_i^{k-1})/\Delta t$$

when $k \geq 1$ and $\mathbf{V}_i^k = \mathbf{v}_0(\mathbf{x}_i)$ when $k = 0$, where \mathbf{v}_0 is the prescribed initial condition for the velocity. From (26), \mathbf{U}^k is computed using, for $k \geq 1$ and all i ,

$$\mathbf{U}_i^{k+1} = \Delta t^2 \frac{\mathbf{F}(\mathbf{u}_h^k)(\mathbf{x}_i) + \mathbf{b}(\mathbf{x}_i, t^k)}{\rho} + 2\mathbf{U}_i^k - \mathbf{U}_i^{k-1} \quad (76)$$

and, for $k = 0$ and all i ,

$$\mathbf{U}_i^1 = \frac{\Delta t^2}{2} \frac{\mathbf{F}(\mathbf{u}_h^0)(\mathbf{x}_i) + \mathbf{b}(\mathbf{x}_i, 0)}{\rho} + \Delta t \mathbf{v}_0(\mathbf{x}_i) + \mathbf{u}_0(\mathbf{x}_i). \quad (77)$$

In the above, the numerical evaluation of peridynamics force $\mathbf{F}(\mathbf{u}_h^k)(\mathbf{x}_i)$ is nontrivial and, therefore, is detailed next.

Algorithm 1 NFEA implementation

```

1: Read nodes and element-node connectivity from the mesh file
2: %% Task: Create neighbor list and compute  $V_{ij}$  using (81)
3: for Each integer  $0 \leq i \leq N - 1$  do %  $N$  is the total number of nodes
4:   for Element  $e \in E_j$  do %  $E_j$  list of elements with node  $j$  as vertex
5:     for  $1 \leq q \leq Q^e$  do % Loop over quadrature points of element  $T_e$ 
6:       if  $|\mathbf{x}_q - \mathbf{X}[i]| \leq \epsilon$  then
7:         Add  $j$  to neighborList[i]
8:         Compute  $V_{ij}$  using (80), add  $V_{ij}$  to  $\mathbf{V}[i]$ 
9:       end if
10:    end for
11:   end for
12: end for % End of loop over nodes for neighborlist
13: %% Task: Integrate in time
14: for Each integer  $0 \leq k \leq t_F/\Delta t$  do
15:   %  $\mathbf{U}, \mathbf{V}$  are the displacement and velocity at step  $k$ 
16:   %% Task: Compute force  $\mathbf{F}$  using (82)
17:   Initialize vector  $\mathbf{F}$  with zeros
18:   for Each integer  $0 \leq i \leq N - 1$  do
19:     for Each integer  $j \in \text{neighborList}[i]$  do
20:        $S_{-ji} = \frac{\mathbf{U}[j] - \mathbf{U}[i]}{|\mathbf{X}[j] - \mathbf{X}[i]|} \cdot \frac{\mathbf{X}[j] - \mathbf{X}[i]}{|\mathbf{X}[j] - \mathbf{X}[i]|}$ 
21:        $\mathbf{F}[i] = \mathbf{F}[i] + \frac{\omega(\mathbf{X}[i])\omega(\mathbf{X}[j])}{w_d \epsilon^{d+1}} \psi'(|\mathbf{X}[j] - \mathbf{X}[i]|) S_{-ji} \frac{\mathbf{X}[j] - \mathbf{X}[i]}{|\mathbf{X}[j] - \mathbf{X}[i]|} V[i][j]$ 
22:     end for
23:   end for % End of loop over nodes for  $\mathbf{F}$ 
24:   %% Task: Update displacement  $\mathbf{U}$  and velocity  $\mathbf{V}$ 
25:   for Each integer  $0 \leq i \leq N - 1$  do
26:     for Each integer  $0 \leq l \leq d - i$  do %  $d$  is the dimension of the problem
27:        $\mathbf{U}_{-temp} = \mathbf{U}[i][l]$ 
28:       if dof  $l$  of node  $i$  is free then
29:          $\mathbf{U}[i][l] = \mathbf{U}[i][l] + \Delta t \mathbf{V}[i][l] + \Delta t^2 \frac{\mathbf{F}[i][l] + \mathbf{b}_{-l}(\mathbf{X}[i], k\Delta t)}{\rho(\mathbf{X}[i])}$ 
30:       else
31:         Read  $\mathbf{U}[i][l]$  from boundary condition
32:       end if
33:        $\mathbf{V}[i][l] = \frac{\mathbf{U}[i][l] - \mathbf{U}_{-temp}[i][l]}{\Delta t}$ 
34:     end for
35:   end for % End of loop over nodes for  $\mathbf{U}$  and  $\mathbf{V}$  update
36: end for % End of loop over time

```

From (10), it holds that

$$\mathbf{F}(\mathbf{u}_h^k)(\mathbf{x}_i) = \sum_{T \in \mathcal{T}_h} \int_{H_\epsilon(\mathbf{x}_i) \cap T} \frac{\omega(\mathbf{x}_i)\omega(\mathbf{y})}{w_d \epsilon^{d+1}} J^\epsilon(|\mathbf{y} - \mathbf{x}_i|) \psi'(|\mathbf{y} - \mathbf{x}_i|) S(\mathbf{y}, \mathbf{x}_i; \mathbf{u}_h^k)^2 S(\mathbf{y}, \mathbf{x}_i; \mathbf{u}_h^k) \frac{\mathbf{y} - \mathbf{x}_i}{|\mathbf{y} - \mathbf{x}_i|} d\mathbf{y}.$$

Let N_T be the list of nodes that are vertices of element T . Recall that ϕ_i denotes the interpolation function of node i . For $\mathbf{y} \in T$, $\mathbf{u}_h^k(\mathbf{y}) = \sum_{j \in N_T} \phi_j(\mathbf{y}) \mathbf{U}_j^k$. Also, for any node i , $\mathbf{u}_h^k(\mathbf{x}_i) = \mathbf{U}_i^k = \sum_{j \in N_T} \phi_j(\mathbf{y}) \mathbf{U}_j^k$ for

all $\mathbf{y} \in T$ (due to the partition of unity property, i.e., $\sum_{j \in N_T} \phi_j(\mathbf{y}) = 1$). Combining, it follows that

$$\begin{aligned} \mathbf{F}(\mathbf{u}_h^k)(\mathbf{x}_i) &= \sum_{T \in \mathcal{T}_h} \left[\sum_{j \in N_T} \int_{H_\epsilon(\mathbf{x}_i) \cap T} \frac{\omega(\mathbf{x}_i)\omega(\mathbf{y})}{w_d \epsilon^{d+1}} J^\epsilon(|\mathbf{y} - \mathbf{x}_i|) \psi'(|\mathbf{y} - \mathbf{x}_i|) S(\mathbf{y}, \mathbf{x}_i; \mathbf{u}_h^k)^2 \right. \\ &\quad \left. \left(\phi_j(\mathbf{y}) \frac{\mathbf{U}_j^k - \mathbf{U}_i^k}{|\mathbf{y} - \mathbf{x}_i|} \cdot \frac{\mathbf{y} - \mathbf{x}_i}{|\mathbf{y} - \mathbf{x}_i|} \right) \frac{\mathbf{y} - \mathbf{x}_i}{|\mathbf{y} - \mathbf{x}_i|} d\mathbf{y} \right]. \end{aligned}$$

Motivated from the above, peridynamics force $\mathbf{F}(\mathbf{u}_h^k)(\mathbf{x}_i)$ can be approximated as follows

$$\begin{aligned} \mathbf{F}(\mathbf{u}_h^k)(\mathbf{x}_i) &\approx \sum_{j \in \text{PD}_i} \frac{\omega(\mathbf{x}_i)\omega(\mathbf{x}_j)}{w_d \epsilon^{d+1}} \psi'(|\mathbf{x}_j - \mathbf{x}_i|) S(\mathbf{x}_j, \mathbf{x}_i; \mathbf{u}_h^k)^2 \left(\frac{\mathbf{U}_j^k - \mathbf{U}_i^k}{|\mathbf{x}_j - \mathbf{x}_i|} \cdot \frac{\mathbf{x}_j - \mathbf{x}_i}{|\mathbf{x}_j - \mathbf{x}_i|} \right) \frac{\mathbf{x}_j - \mathbf{x}_i}{|\mathbf{x}_j - \mathbf{x}_i|} \\ &\quad \left[\sum_{e \in E_j} \int_{H_\epsilon(\mathbf{x}_i) \cap T_e} J^\epsilon(|\mathbf{y} - \mathbf{x}_i|) \phi_j(\mathbf{y}) d\mathbf{y} \right], \end{aligned} \quad (78)$$

where, E_j is the list of elements with node j as its vertex, see Fig. 3, and PD_i is the list of neighboring nodes j and it is defined as

$$\text{PD}_i := \{1 \leq j \leq N : T_e \cap H_\epsilon(\mathbf{x}_i) \neq \emptyset \text{ for at least one } e \in E_j\}. \quad (79)$$

Note that $\{1 \leq j \leq N : \mathbf{x}_j \in H_\epsilon(\mathbf{x}_i)\} \subset \text{PD}_i$, i.e., PD_i consists of nodes that are in the horizon $H_\epsilon(\mathbf{x}_i)$ and additional nodes outside $H_\epsilon(\mathbf{x}_i)$ which may belong to element T_e that intersects $H_\epsilon(\mathbf{x}_i)$. The above form of approximation is not unique, as one may also approximate the force as

$$\begin{aligned} \mathbf{F}(\mathbf{u}_h^k)(\mathbf{x}_i) &\approx \sum_{j \in \text{PD}_i} \frac{\omega(\mathbf{x}_i)\omega(\mathbf{x}_j)}{w_d \epsilon^{d+1}} \left(\frac{\mathbf{U}_j^k - \mathbf{U}_i^k}{|\mathbf{x}_j - \mathbf{x}_i|} \cdot \frac{\mathbf{x}_j - \mathbf{x}_i}{|\mathbf{x}_j - \mathbf{x}_i|} \right) \frac{\mathbf{x}_j - \mathbf{x}_i}{|\mathbf{x}_j - \mathbf{x}_i|} \\ &\quad \left[\sum_{e \in E_j} \int_{H_\epsilon(\mathbf{x}_i) \cap T_e} \psi'(|\mathbf{y} - \mathbf{x}_i|) S(\mathbf{y}, \mathbf{x}_i; \mathbf{u}_h^k)^2 J^\epsilon(|\mathbf{y} - \mathbf{x}_i|) \phi_j(\mathbf{y}) d\mathbf{y} \right]. \end{aligned}$$

Similarly, other forms of approximation are possible by keeping some terms outside and some inside of the integration. In our implementation, the approximation (78) is used for two reasons: 1. The term in the square bracket is independent of time and, therefore, can be computed only once in the beginning and stored, and 2. The choice of keeping nonlinear term outside the integral as well as the vector $(\mathbf{x}_j - \mathbf{x}_i)/|\mathbf{x}_j - \mathbf{x}_i|$ gives a stable simulation, and numerical results agree well with the benchmark problems. Proceeding further, let V_{ij} be the weighted volume of a node j for a pairwise force contribution to the node i . It is defined as

$$V_{ij} = \sum_{e \in E_j} \int_{H_\epsilon(\mathbf{x}_i) \cap T_e} J^\epsilon(|\mathbf{y} - \mathbf{x}_i|) \phi_j(\mathbf{y}) d\mathbf{y}. \quad (80)$$

The above integration over an element is computed using the quadrature rule. In all the numerical results, the second-order quadrature rule is employed; higher-order schemes can be used as the above integration needs to be computed only once and stored in the memory. Let Q^e be the number of quadrature points associated with the element e (e is the element number, and T_e is the element). Further, let, for $q = 1, \dots, Q^e$, (\mathbf{x}_q, w_q) is the pair of quadrature points and weights. Then

$$V_{ij} = \sum_{e \in E_j} \left[\sum_{q=1}^{Q^e} \chi_{H_\epsilon(\mathbf{x}_i)}(\mathbf{x}_q) J^\epsilon(|\mathbf{x}_q - \mathbf{x}_i|) \phi_j(\mathbf{x}_q) w_q \right], \quad (81)$$

Properties	Values	Properties	Values
ρ (kg/m^3)	1200	c_L (m/s)	6123.7
E (GPa)	37.5	c_S (m/s)	3535.5
G_c (J/m^2)	500	c_R (m/s)	3244.2

Table 1: Material properties. Formulae in (84) are used to compute longitudinal (c_L), shear (c_S), and Rayleigh (c_R) wave speeds.

where $\chi_A(\mathbf{x})$ is the indicator function taking value 1 if $\mathbf{x} \in A$ and 0 if $\mathbf{x} \notin A$. Using the definition of V_{ij} , (78) can be written as

$$\mathbf{F}(\mathbf{u}_h^k)(\mathbf{x}_i) \approx \sum_{j \in \text{PD}_i} \frac{\omega(\mathbf{x}_i)\omega(\mathbf{x}_j)}{w_d \epsilon^{d+1}} \psi'(|\mathbf{x}_j - \mathbf{x}_i|) S(\mathbf{x}_j, \mathbf{x}_i; \mathbf{u}_h^k)^2 \left(\frac{\mathbf{U}_j^k - \mathbf{U}_i^k}{|\mathbf{x}_j - \mathbf{x}_i|} \cdot \frac{\mathbf{x}_j - \mathbf{x}_i}{|\mathbf{x}_j - \mathbf{x}_i|} \right) \frac{\mathbf{x}_j - \mathbf{x}_i}{|\mathbf{x}_j - \mathbf{x}_i|} V_{ij}. \quad (82)$$

In Fig. 3, one of the neighboring nodes \mathbf{x}_j contributing to the force at \mathbf{x}_i is shown on an example 2-d finite element mesh. Algorithm 1 presents the implementation of NFEA.

7.2. Material properties

Let ρ denote the density, E Young's modulus, ν Poisson ratio, and G_c critical energy release rate. The bond-based peridynamics suffer from the restriction of Poisson ratio $\nu = 1/4$ in 3-d or 2-d plane strain and $\nu = 1/3$ in 2-d plane stress; see Trageser and Seleson (2020). All of the simulations are in 2-d, and plane strain is assumed. Therefore, ν is fixed to 1/4.

To fix the parameters in the RNP model, see (9), the nonlinear potential function ψ is set to $\psi(r) = c(1 - \exp[-\beta r])$, where c and β are two model parameters. The influence function is taken to be $J^\epsilon(r) = J(r/\epsilon)$, where $J(r) = 1 - r$ for $0 \leq r < 1$ and $J(r) = 0$ for $r \geq 1$. The boundary function $\omega(\mathbf{x})$ is taken as 1 for all points \mathbf{x} in the domain, i.e., $\omega(\mathbf{x}) = 1$ for $\mathbf{x} \in D$. Given E , Lamé parameter are $\lambda = \mu = 2E/5$ ($\nu = 1/4$ is assumed). The parameters c and β , in 2-d, can be determined from (see Lipton (2016))

$$c = \frac{G_c \pi}{4M_J}, \quad \beta = \frac{8E}{5cM_J}, \quad (83)$$

where, $M_J = \int_0^1 J(r)r^2 dr = 1/12$ for $J(r) = 1 - r$. The inflection point of the potential function ψ is given by $r^* = 1/\sqrt{2\beta}$ and the critical strain $S_c(\mathbf{y}, \mathbf{x}) = \pm r^*/\sqrt{|\mathbf{y} - \mathbf{x}|}$.

Let c_L , c_S , and c_R are the longitudinal, shear, and Rayleigh wave speeds, respectively. Given elastic properties such as E and ν , wave speeds can be computed using the formulae:

$$c_L = \sqrt{\frac{\lambda + 2\mu}{\rho}} = \sqrt{\frac{1 - E(1 - \nu)}{\rho(1 + \nu)(1 - 2\nu)}}, \quad c_S = \sqrt{\frac{\mu}{\rho}} = \sqrt{\frac{1}{\rho} \frac{E}{2(1 + \nu)}}, \quad c_R \approx c_S \left(\frac{0.862 + 1.14\nu}{1 + \nu} \right), \quad (84)$$

where the last formula to approximate Rayleigh wave speed can be found in Royer and Clorennec (2007). Material properties employed in numerical experiments are listed in Table 1.

Definition 7.1 (Damage). *The damage at the material point \mathbf{x} is defined as*

$$Z(\mathbf{x}) := \sup_{\mathbf{y} \in H_\epsilon(\mathbf{x}) \cap D} \frac{|S(\mathbf{y}, \mathbf{x})|}{|S_c(\mathbf{y}, \mathbf{x})|}. \quad (85)$$

Based on the above, if $Z(\mathbf{x}) \geq 1$, it follows that \mathbf{x} has at least one bond in the neighborhood with the bond strain above the critical bond strain. The damage zone of the material is given by the set $\{\mathbf{x} \in D : Z(\mathbf{x}) \geq 1\}$. Other measures of damage are also possible. For example, consider a function φ given by

$$\varphi(\mathbf{x}) = \frac{\int_{H_\epsilon(\mathbf{x}) \cap D} \mu(\mathbf{y}, \mathbf{x}; S) d\mathbf{y}}{\int_{H_\epsilon(\mathbf{x}) \cap D} d\mathbf{y}}, \quad (86)$$

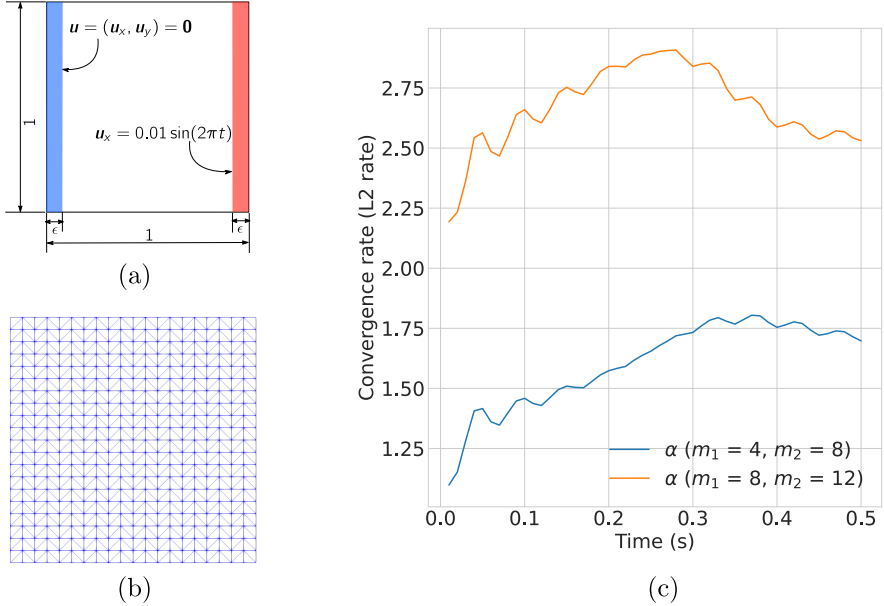


Figure 4: (a) **Convergence test**: Setup. The horizon is fixed to $\epsilon = 0.05$ m. (b) A representative view of the mesh consisting of linear triangle elements. (c) Rate of convergence at discrete times using (87).

where, $\mu(\mathbf{y}, \mathbf{x}; S)$ is a function that models the breakage of bond:

$$\mu(\mathbf{y}, \mathbf{x}; S) = \begin{cases} 1, & \text{if } S(\mathbf{y}, \mathbf{x}) < S_c(\mathbf{y}, \mathbf{x}), \\ 0, & \text{otherwise.} \end{cases}$$

Thus, $\varphi(\mathbf{x}) \in [0, 1]$, and $\varphi(\mathbf{x}) = 0$ implies all the bonds in the neighborhood of \mathbf{x} are stretched below the critical value, while $\varphi(\mathbf{x}) = 1$ implies all the bonds in the neighborhood have strains above the critical value.

Remark 7.2. The plots of fields, such as damage, displacement, and linearized strain (symmetric gradient of displacement), are based on the finite element representation (surface plot in Paraview) and are in a deformed configuration unless otherwise stated in the figure's caption. The strain field is a piecewise constant over elements, and the strain value in each element is computed at the element's center.

The field $Z(\mathbf{x})$ is displayed using two colors (blue and red) to visualize damage. The blue color means $Z(\mathbf{x}) \leq 1$ and the point \mathbf{x} is colored red if $Z(\mathbf{x}) := \max_{\mathbf{y} \in H_\epsilon(\mathbf{x})} |S(\mathbf{y}, \mathbf{x})| / S_c(\mathbf{y}, \mathbf{x}) > 1$, i.e., red colored point \mathbf{x} has at least one neighboring point \mathbf{y} such that the bond $\mathbf{x} - \mathbf{y}$ is stretched above the threshold stretch. Thus, red indicates that the point has at least one critically stretched bond.

7.3. Convergence test on square domain with displacement controlled loading

A simple example of displacement-controlled loading is considered to test the convergence of the Nodal FE approximation. Consider a two-dimensional solid body $D = [0, 1m]^2$ with density $\rho = 1$ kg/m³, Young's modulus $E = 1$ Pa, and Poisson ratio $\nu = 0.25$. Thickness is one meter, and the horizon is fixed to $\epsilon = 0.05$ m. The left layer of specimens of ϵ thickness is clamped (zero displacements in x and y directions). The layer on the right of thickness ϵ is subjected to displacement $u_x(\mathbf{x}, t) = 0.01 \sin(2\pi t)$ in the x direction while the displacement in the y direction is kept free; see Fig. 4(a). To test the convergence, four different mesh sizes are considered: $h_i = \epsilon/m_i$ for $i = 1, 2, 3, 4$ with $m_1 = 4, m_2 = 8, m_3 = 12, m_4 = 16$. The domain is discretized into the uniform grid, and each grid is further divided into two triangles; see representative mesh in Fig. 4(b). The size of the grid is the mesh size. The final simulation time is $t_F = 0.5$ s, the time step size $\Delta t = 0.000125$ s, and the results are written to file every $\Delta t_{out} = 0.01$ s interval.

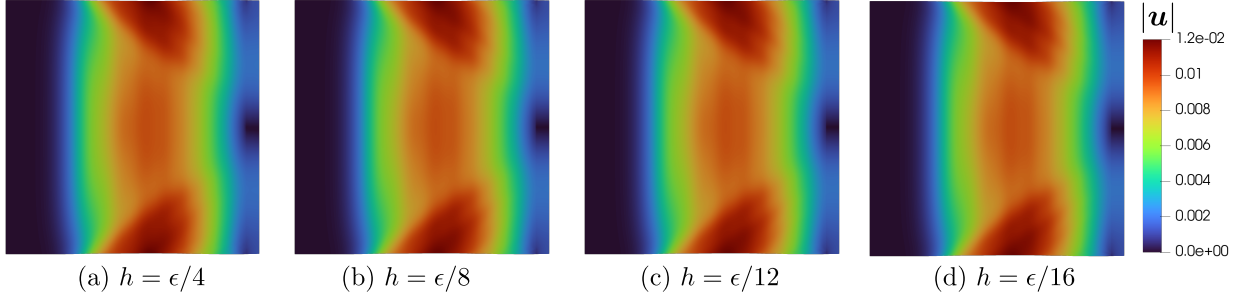


Figure 5: **Convergence test:** Comparing the magnitude of displacement at the final simulation time t_F for all four meshes. Unless otherwise stated, all the plots, including this figure, are in the deformed configuration and based on the finite element representation.

To calculate the convergence rate with mesh refinement, numerical solution $\mathbf{u}_{h_4}(t_k)$ corresponding to the finest mesh is treated as an exact solution, where t_k , $k = 1, 2, \dots, t_F/\Delta t_{out}$, is the output time (time at which solutions are written to a file). Setting $\mathbf{u} = \mathbf{u}_{h_4}$, the rate of convergence at a time t_k from two solutions $\mathbf{u}_{h_i}(t_k)$ and $\mathbf{u}_{h_{i+1}}(t_k)$ can be computed as follows:

$$\alpha(t^k) = \frac{\log(||\mathbf{u}_{h_i}(t_k) - \mathbf{u}(t_k)||) - \log(||\mathbf{u}_{h_{i+1}}(t_k) - \mathbf{u}(t_k)||)}{\log(h_i) - \log(h_{i+1})}. \quad (87)$$

Using the numerical solutions for three mesh sizes $h_1 = \epsilon/m_1, h_2 = \epsilon/m_2, h_3 = \epsilon/m_3$ (h_4 is used as an “exact” solution), convergence rates $\alpha(t_k; m_1, m_2)$ and $\alpha(t_k; m_2, m_3)$ at output times t_k , $k = 1, 2, \dots, t_F/\Delta t_{out}$, are computed and displayed in Fig. 4(c). Results show that the convergence rate is quite good and above 2 as the mesh size is reduced from $\epsilon/8$ to $\epsilon/12$. When reducing the mesh size from $\epsilon/4$ to $\epsilon/8$, the convergence rate is above 1.5 and below the optimal rate of 2 from the a-priori error analysis. These rates, however, are excellent considering that the NFEA is similar to the meshfree discretization and approximates the nodal peridynamics forces using a discrete summation of node-node interaction (integration through the quadrature method will increase the computational cost). In Fig. 5, the magnitude of the displacement field is displayed for four simulations with different mesh sizes at the final time $t_F = 0.5$ s. Visually, all the results are in agreement.

7.4. Mode-I crack propagation

Consider a square domain $D = [0, 100 \text{ mm}]^2$ with a vertical pre-crack of length $l = 20 \text{ mm}$ located at the center; see Fig. 6a(a). If a specimen has a pre-crack line/curve (surface in 3-d), it means that in the peridynamics simulation, all the bonds intersecting the pre-crack line/curve (surface in 3-d) are initially broken and are kept broken during the course of the simulation. The constant velocity of $\pm 10^3 \text{ mm/s}$ is specified on the small area on the left and right sides to obtain the mode-I crack propagation. The simulation time and the size of the time step are $t_F = 40 \mu\text{s}$ and $\Delta t = 0.0008 \mu\text{s}$, respectively, and the output is written to a file every $\Delta t_{out} = t_F/50$ interval. The nonlocal length-scale, i.e., horizon, is fixed to $\epsilon = 2 \text{ mm}$. In the simulations, the RNP model with the material properties listed in Table 1 is employed.

As in the previous example, to get the estimated convergence rate with mesh refinement, discretized solutions for mesh sizes $h_i = \epsilon/m_i$, $i = 1, 2, 3, 4$, with $m_1 = 4, m_2 = 8, m_3 = 12, m_4 = 16$ are computed. The finite element solution $\mathbf{u}_{h_4}(t_k)$ corresponding to the finest mesh, i.e., $h = h_4 = \epsilon/16$, is employed as an exact solution $\mathbf{u}(t_k) = \mathbf{u}_{h_4}(t_k)$, and using simulation results $\mathbf{u}_{h_1}(t_k), \mathbf{u}_{h_2}(t_k), \mathbf{u}_{h_3}(t_k)$, convergence rates $\alpha(t_k; m_1, m_2)$ and $\alpha(t_k; m_2, m_3)$ at output times t_k , $k = 1, 2, \dots, t_F/\Delta t_{out}$, are computed following (87). Note that m_1 and m_2 in $\alpha(\cdot; m_1, m_2)$ indicate that the rate is for meshes $h_1 = \epsilon/m_1$ and $h_2 = \epsilon/m_2$. Two convergence rates, $\alpha(\cdot; m_1, m_2)$ and $\alpha(\cdot; m_2, m_3)$, are shown in Fig. 6b. In Fig. 7, the fields \mathbf{u}_x and Z are compared for four meshes at time $t = 28 \mu\text{s}$. The results show that the plots are visually indistinguishable.

Next, the plot of the damage function Z defined in (85) is presented in the left column of Fig. 8. In the right column, linearized strain is computed from the displacement field, and its magnitude (magnitude of

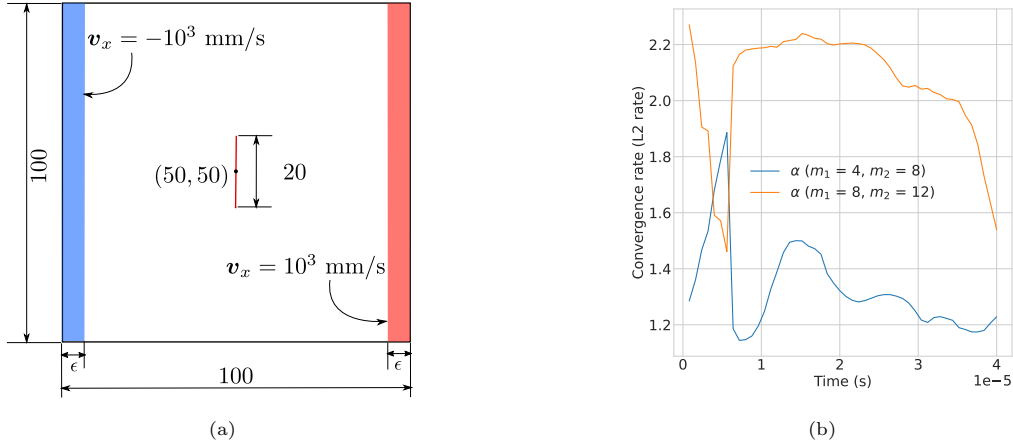


Figure 6: (a) **Mode-I crack problem:** Setup. The horizon is $\epsilon = 2$ mm. The center of the pre-crack coincides with the center of the domain. (b) **Mode-I crack problem:** Convergence rate as the mesh is refined.

the strain tensor $\mathbf{E} = \frac{1}{2} [\nabla \mathbf{u} + \nabla \mathbf{u}^T]$ is taken as $\|\mathbf{E}\| = \sqrt{\mathbf{E} : \mathbf{E}}$, where $\mathbf{E} : \mathbf{E} = E_{ij}E_{ij}$ is the dot product) is depicted. In all the numerical results, it is found that the width of the process zone (damaged region) is approximately twice the horizon and envelopes the crack interface. Further, the strain tensor magnitude is unusually higher at the crack interface, as expected. To show crack opening, in Fig. 9, the displacement is magnified by a factor of 100 and added to the reference configuration, and the damage Z is displayed in the new artificial deformed configuration.

7.4.1. Comparing NFEA with meshfree method

To validate NFEA by comparing with the existing meshfree method employed in Silling and Askari (2005); Lipton et al. (2019); Jha and Lipton (2019), the present problem of mode-I fracture is used. Specifically, for the mesh size $h = \epsilon/8$, the peridynamics equation is solved using NFEA and the meshfree method. The rest of the parameters and the setup are the same as above. The plots of the damaged region ($Z(\mathbf{x})$) are presented in Fig. 10. The figure shows that the NFEA produces results similar to those of the meshfree method.

7.4.2. Localization of damage

The mode-I fracture problem from the above is employed to show that NFEA can capture the localization of damage and convergence with respect to the nonlocal length scale. To allow comparisons of results for different nonlocal length scales, in the setup of the mode-I fracture problem in Fig. 6a, the thickness of the left and right layers (where displacement boundary condition is applied) is fixed to 3 mm, i.e., the thickness of the layers does not change with the nonlocal length scale. Keeping the rest of the setup details the same, including the final time and time step size, the mode-I fracture is simulated for three horizons $\epsilon \in 3, 2, 1$ mm. Given a horizon ϵ , the mesh size is fixed to $h = \epsilon/4$. In Fig. 11, the damaged region $Z(\mathbf{x}) > 1$ is compared for three horizons at sample times. The results show damage localization as the nonlocal length scale is refined. Most importantly, points on the left of the localized damage zone do not interact with those on the right, and we have formed a piece of crack.

7.5. Material with a circular hole subjected to an axial loading

A material with a hole, as shown in Fig. 12, is subjected to displacement-controlled axial pulling. The details of the setup and boundary conditions are given in Fig. 12. The remaining parameters are fixed as follows: horizon $\epsilon = 1$ mm, mesh size $h = 0.25$ mm, final time of the simulation $t_F = 160 \mu\text{s}$, and the size of the time step $\Delta t = 0.0016 \mu\text{s}$. Peridynamics force is computed using the RNP model.

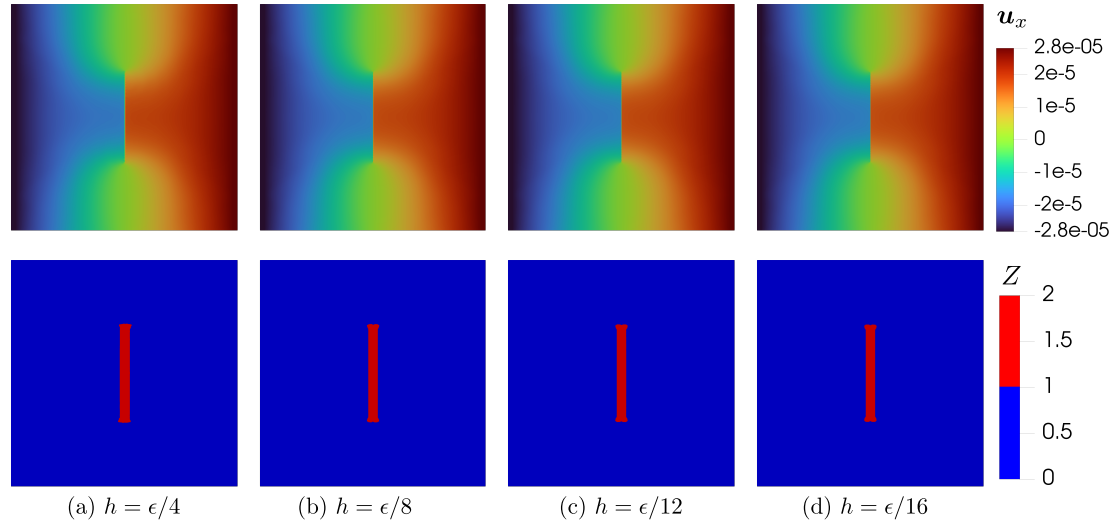


Figure 7: **Mode-I crack problem:** Comparing u_x and Z fields for different mesh sizes at time $t = 28\mu\text{s}$. In the bottom row for the plots of damage field Z , note that the red indicates that the point has at least one critically stretched bond; see [Theorem 7.2](#).

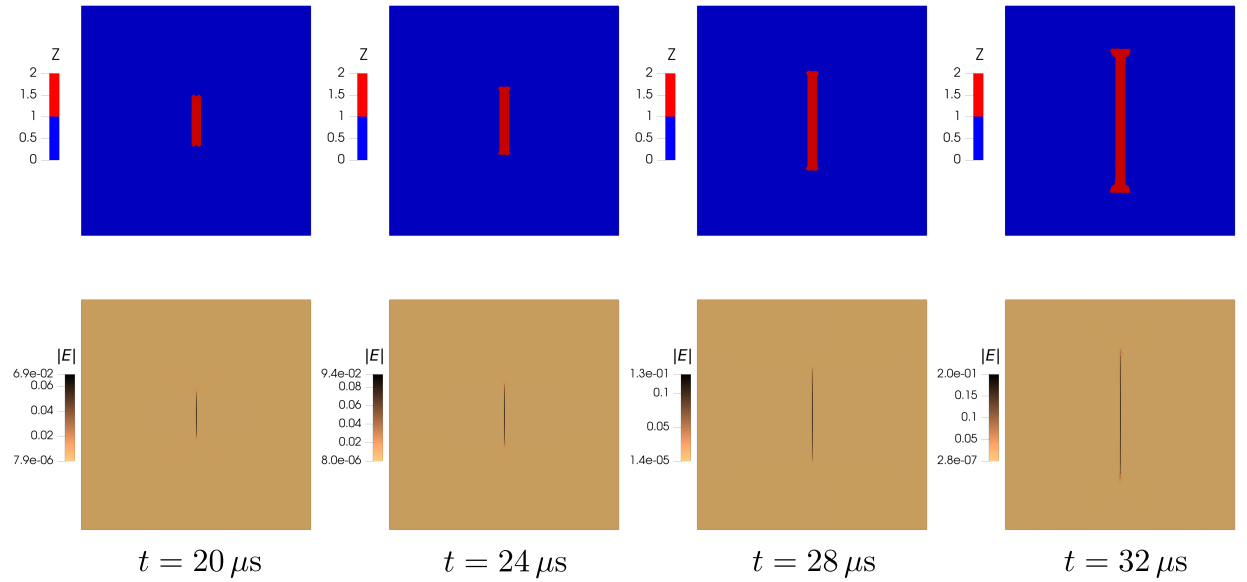


Figure 8: **Mode-I crack problem:** Plot of damage (**top row**) and the magnitude of the strain $\mathbf{E} = \frac{1}{2} [\nabla \mathbf{u} + \nabla \mathbf{u}^T]$ (**bottom row**). The damage and strains are localized near the crack interface. The thickness of the damage zone in the left column (red region) is approximately twice the horizon. Since the finite element displacement is continuous and piecewise linear, the strain tensor field over each element is constant, and the value is computed at the element's center.

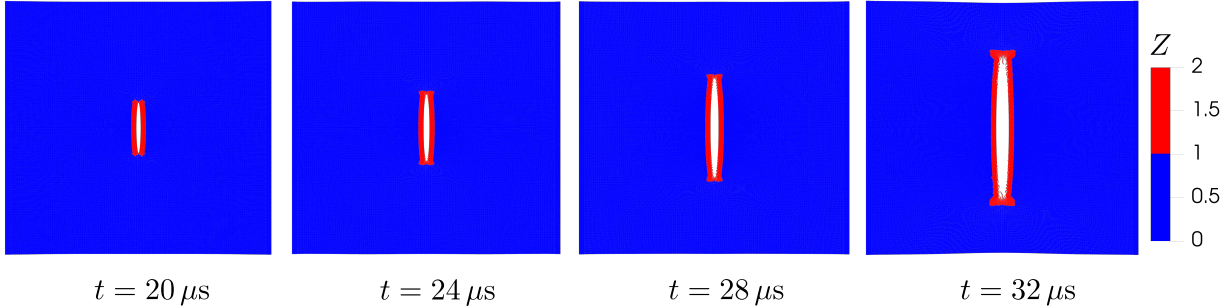


Figure 9: **Mode-I crack problem:** Plot of damage in the deformed configuration after scaling the displacement field by 100 to show the crack opening. The plots are obtained using the nodal data (without finite element representation) to show a clear opening. This procedure is repeated in other figures where the opening is visualized by scaling the displacement field.

The damage profile and the strains are presented in Fig. 13. Crack nucleation is seen when the internal stresses become large enough. It is also clear that the crack nucleates at the top and bottom edges of the void where the stresses are most significant; see Fig. 13(e). To visualize crack opening and branching, the displacement field is magnified by a factor of 50 in Fig. 21. Branching of the cracks is also seen at later times.

7.6. Material with a v-notch under bending load

In this example, a rectangle beam with a v-notch is subjected to the bending load as shown in Fig. 15. The horizon is fixed to $\epsilon = 1$ mm, mesh size $h = 0.25$ mm, final simulation time $t_F = 250 \mu\text{s}$, and the size of the time step $\Delta t = 0.001667 \mu\text{s}$. Peridynamics force is based on the RNP model.

The damage profile and the magnitude of the strain are presented in Fig. 16. As expected, the crack nucleates at the tip of the notch where the strain is most significant. Similar to the previous example, displacement is magnified by 50 to highlight the separation of the structure in Fig. 17.

7.7. Material with a circular hole and pre-crack

As a final example, a rectangular domain with an existing horizontal pre-crack and a circular hole in the neighborhood of a crack is considered. The setup, as shown in Fig. 18, is motivated by a similar example in Dai et al. (2015). The horizon is fixed to $\epsilon = 0.4$ mm, mesh size $h = 0.1$ mm, the final simulation time $t_F = 800 \mu\text{s}$, and the size of the time step $\Delta t = 0.004 \mu\text{s}$. The peridynamics force is computed using the RNP model.

Damage and the magnitude of the strain at different times are displayed in Fig. 19. Initially, crack propagation is influenced by the hole nearby, and instead of growing horizontally, it is deflected. At later times, when the crack tip moves past the hole, the crack propagates horizontally. A similar problem was considered in (Dai et al., 2015, Figure 18), where results using different numerical methods were compared. The results of this work qualitatively agree with that in Dai et al. (2015). In Fig. 20, strain fields at different times are presented. Opening of the crack is visualized in Fig. 21.

7.8. On the crack propagation speed

In this subsection, the crack propagation speeds from four problems are compared. Let t_1 and t_2 be times when the crack begins and stops propagating, respectively. Also, let $v(t)$, for $t \in [t_1, t_2]$, be the crack speed computed from the simulation at time t . To plot the crack speeds for all four examples in one plot, time $t \in [t_1, t_2]$ is transformed to $\bar{t} = (t - t_1)/(t_2 - t_1)$ so that $\bar{t} \in [0, 1]$. Let $\bar{v}(\bar{t}) = v(t)$ be the crack speed as a function of normalized time \bar{t} . Next, crack speed is normalized by dividing the Rayleigh wave speed c_R ; c_R from Table 1 is 3244.2 m/s.

Fig. 22 presents the normalized crack speed as a function of normalized time for the four problems. As expected, the normalized crack speeds are below 1, i.e., the crack propagates slower than the Rayleigh wave speed; see Table 2, which lists the maximum and average values of normalized crack speeds.

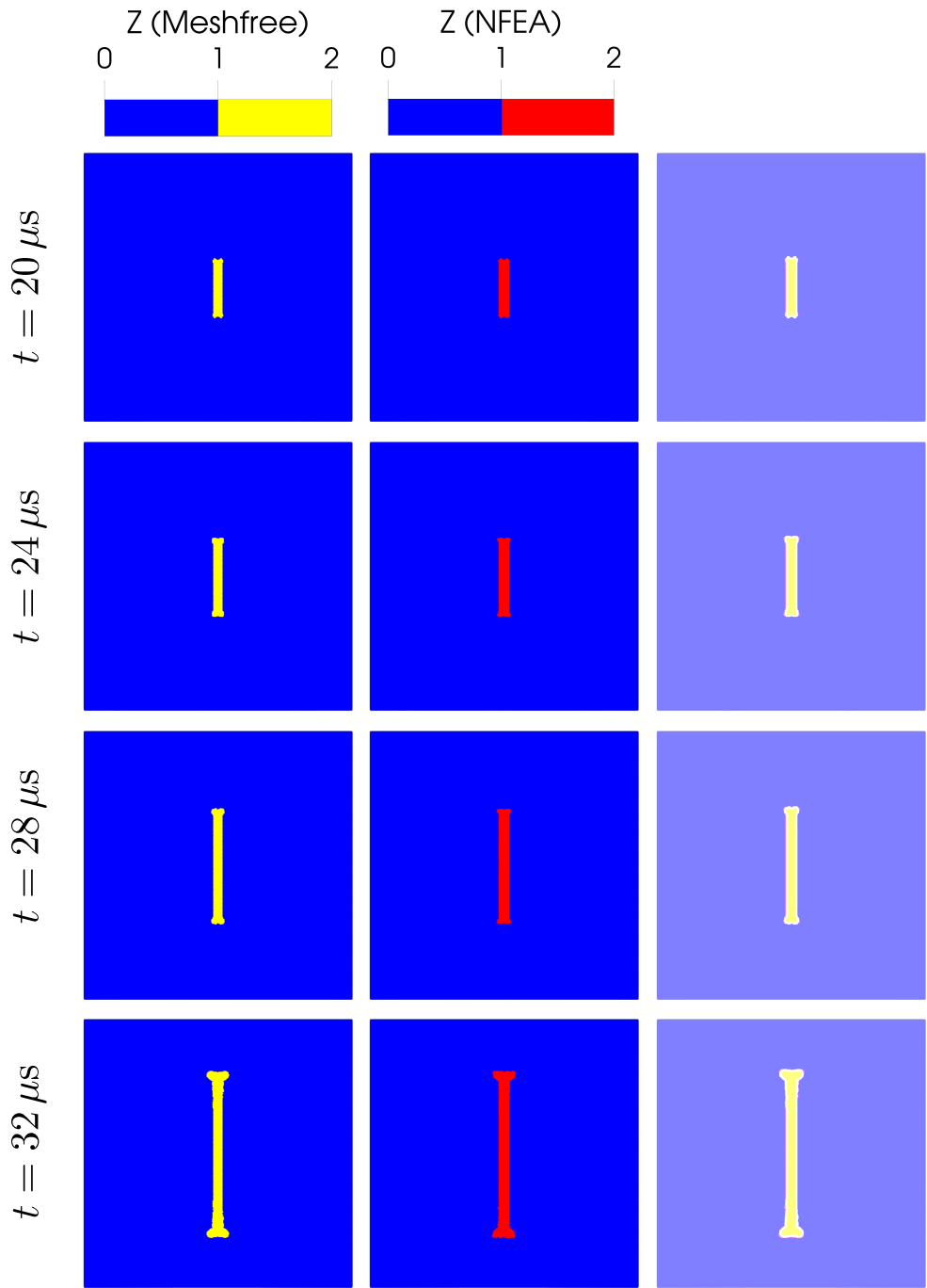


Figure 10: **Mode-I crack problem:** Comparing NFEA and meshfree results for the mode-I fracture problem. Here, the first column plots the damaged zone from the meshfree method, the second column from NFEA, and the overlap of the damaged regions from the two methods is presented in the last column; the opacity of both plots is set to 50% in the overlap plot. The rows correspond to the results at different times. From the plots in the third column, it is clear that the damaged regions from both methods are quite close.

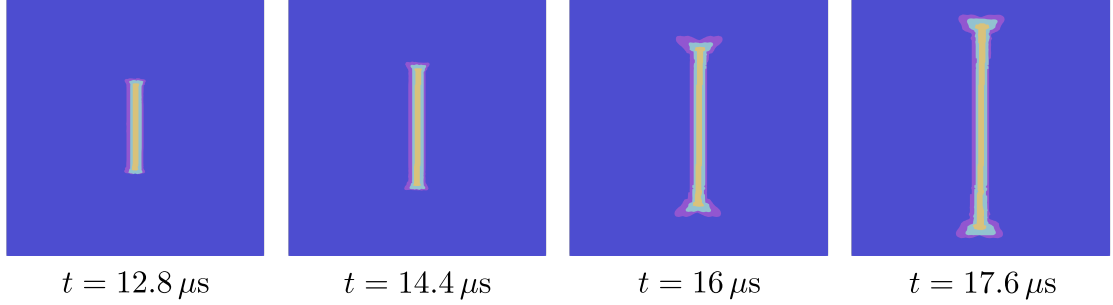


Figure 11: **Mode-I crack problem with fixed thickness of boundary condition layers:** Comparing damaged zone for three different horizons at fixed times. The damaged region $Z(\mathbf{x}) > 1$ shown in color other than blue is overlapped for three horizons, $\epsilon \in \{3, 2, 1\}$ mm. Light yellow, cyan, and purple regions correspond to $\epsilon = 3$ mm, $\epsilon = 2$ mm, and $\epsilon = 1$ mm, respectively. It is seen that the damaged region corresponding to the smallest horizon is contained inside the damaged region for the largest horizon. This demonstrates the localization of damage as ϵ is reduced.

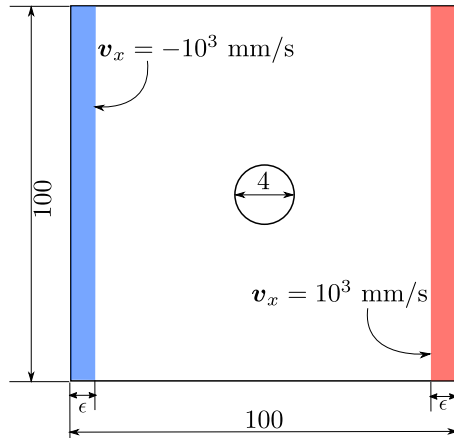


Figure 12: **Circular hole problem:** Setup. The horizon is $\epsilon = 1$ mm. Constant velocity in the opposite direction is specified along the x-axis in the left (blue) and right (red) layers.

Problem type	$\max\left(\frac{v}{c_R}\right)$	$\text{avg}\left(\frac{v}{c_R}\right)$		Problem type	$\max\left(\frac{v}{c_R}\right)$	$\text{avg}\left(\frac{v}{c_R}\right)$
Mode-I crack	0.9	0.51		Circular hole	0.95	0.52
V-notch	0.47	0.22		Circular hole with pre-crack	0.32	0.04

Table 2: Maximum and average normalized crack speeds for the four numerical problems.

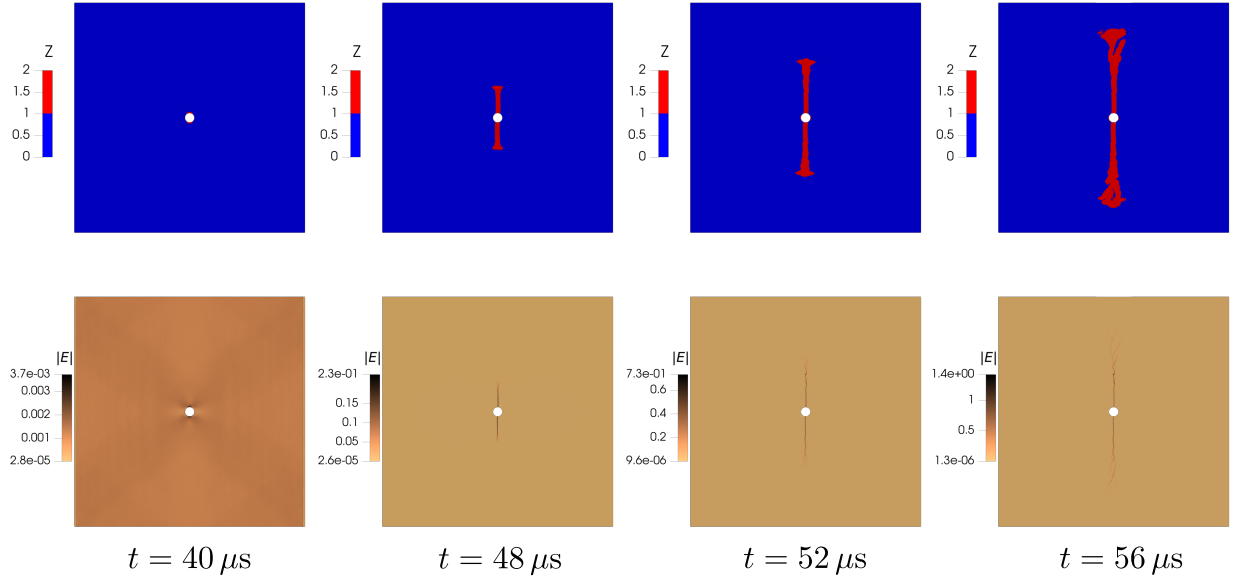


Figure 13: **Circular hole problem:** Plot of damage (**top row**) and the magnitude of the strain $\mathbf{E} = \frac{1}{2} [\nabla \mathbf{u} + \nabla \mathbf{u}^T]$ (**bottom row**). A crack is seen nucleating at the two points on the hole's edge where the strain is maximum.

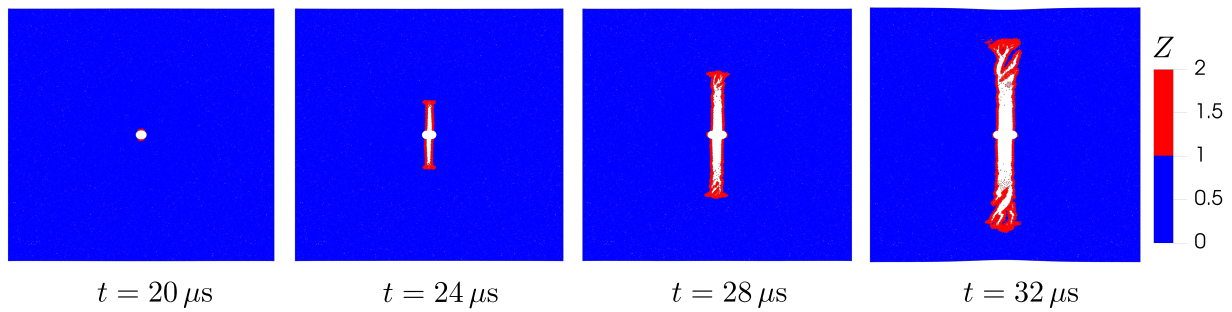


Figure 14: **Circular hole problem:** Plot of damage in the deformed configuration after scaling the displacement field by 50 to show the crack opening.

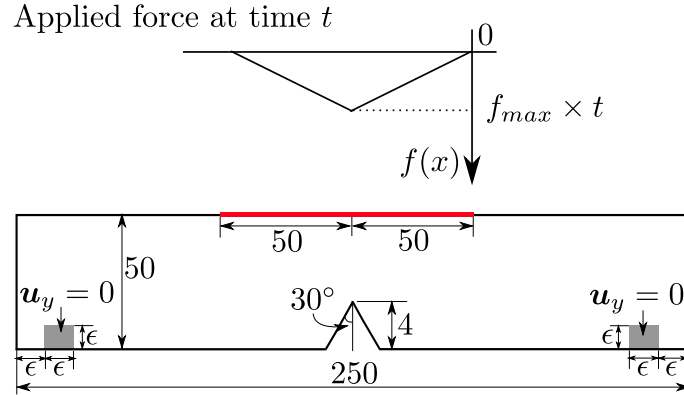


Figure 15: **V-notch problem:** Setup. The horizon in this problem is $\epsilon = 1$ mm. Vertically downward distributed force is applied on the part of the top edge, as shown in red. The profile of distributed load is shown above the red line, where the loading parameter f_{max} is set to $f_{max} = 2.5 \times 10^5$ N/(μ s·mm).

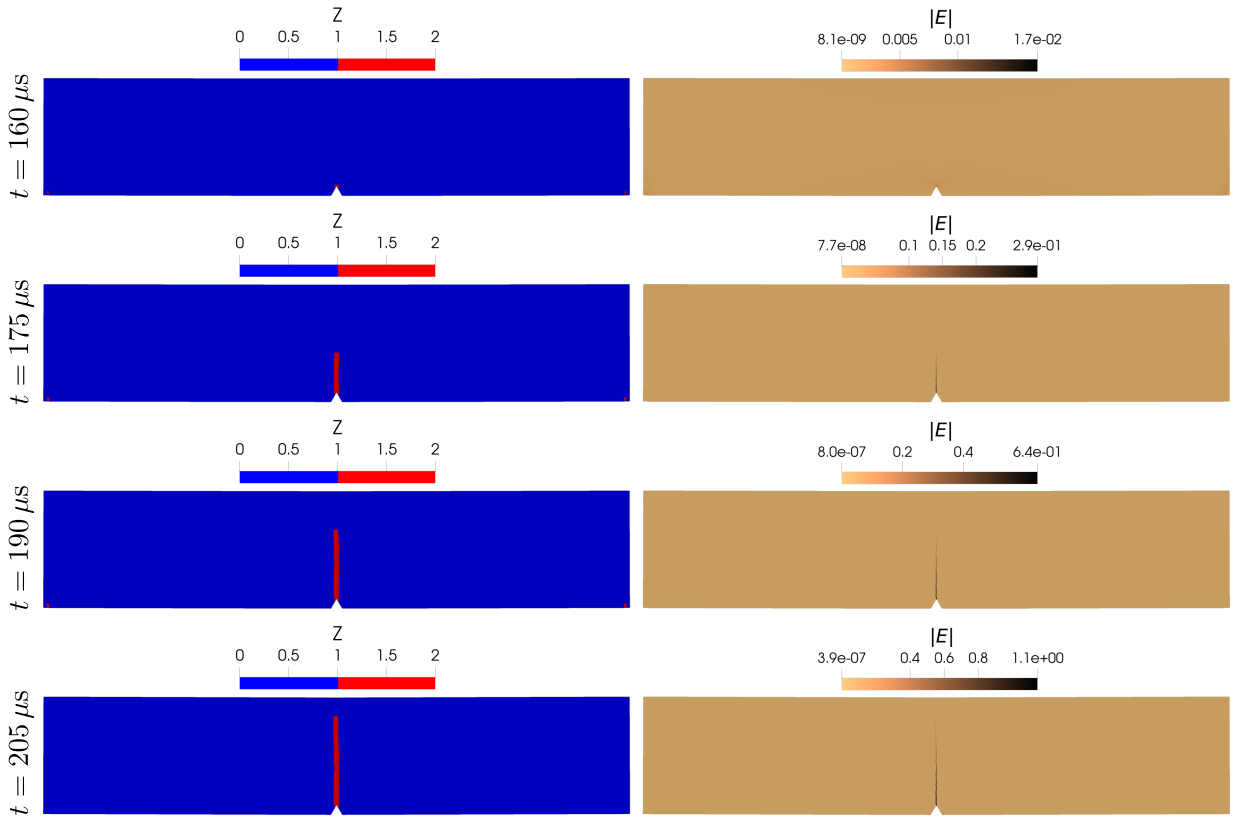


Figure 16: **V-notch problem:** Plot of damage and the magnitude of the strain. Crack nucleates at the tip of the notch where the strain is maximum.

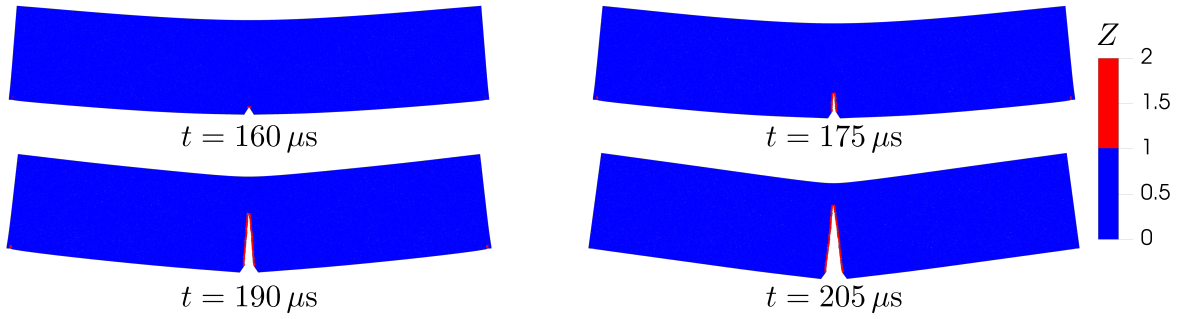


Figure 17: **V-notch problem:** Plot of damage in the deformed configuration after scaling the displacement field by 50 to highlight the separation of the structure.

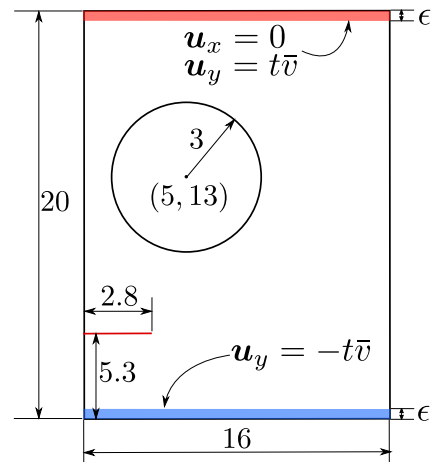


Figure 18: **Circular hole and pre-crack problem:** Setup. The horizon is $\epsilon = 0.4$ mm. The magnitude of the prescribed vertical velocity on the top and bottom layers is $\bar{v} = 25$ mm/s.

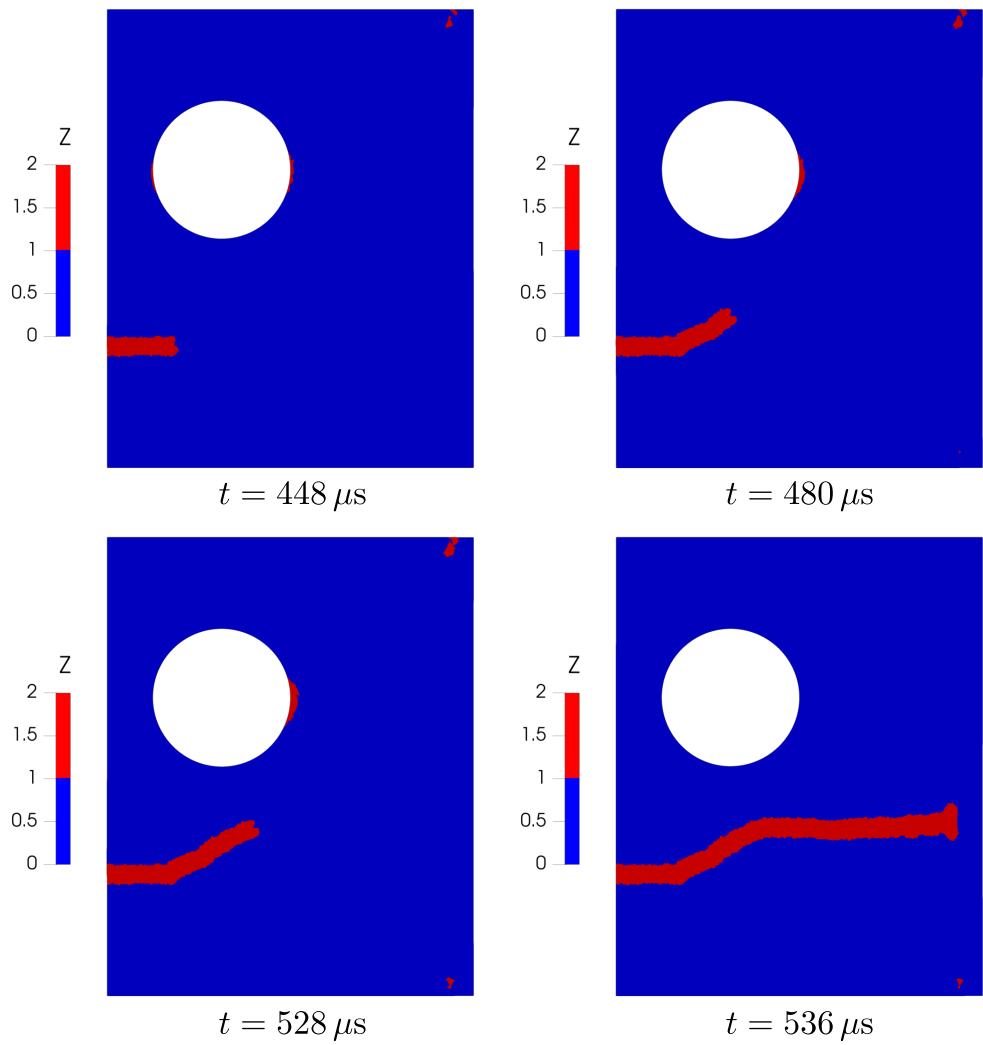


Figure 19: **Circular hole and pre-crack problem:** Plot of damage.

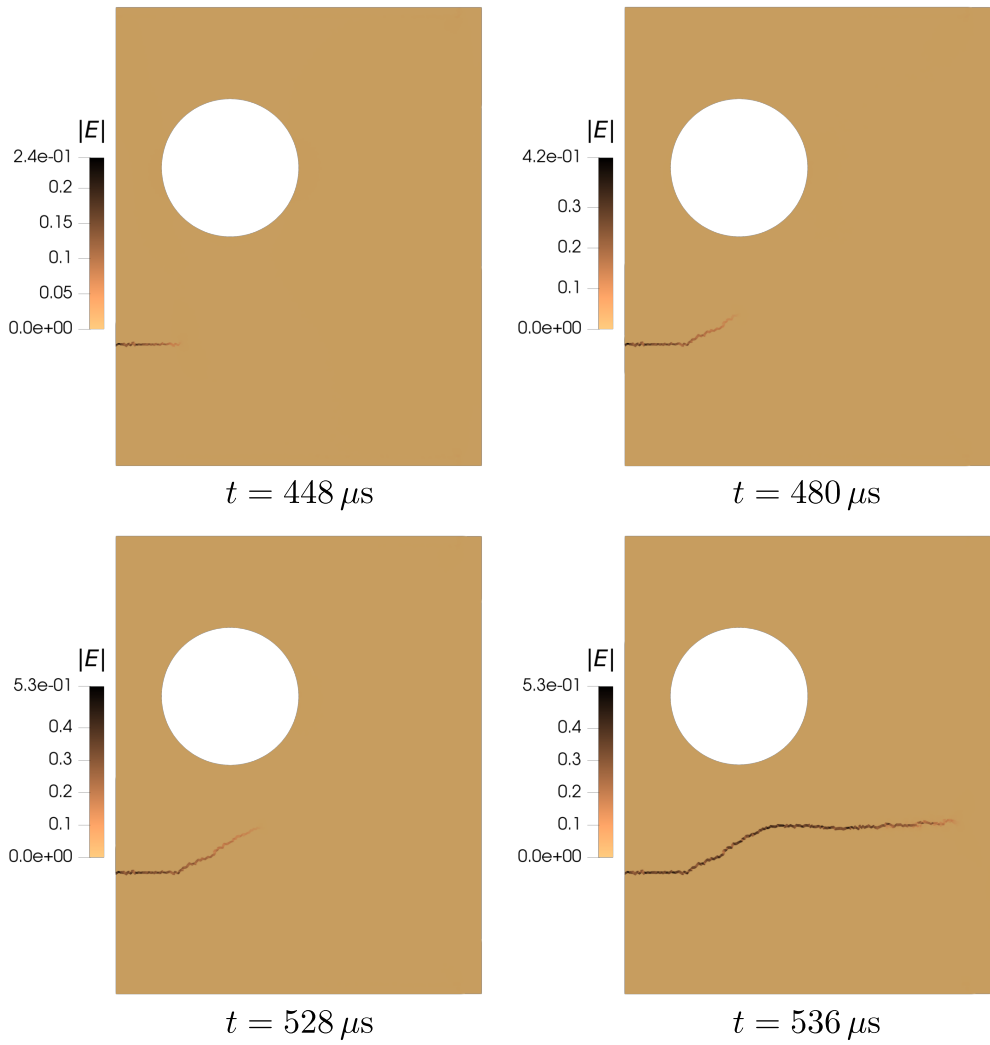


Figure 20: **Circular hole and pre-crack problem:** Plot of the magnitude of strain $\mathbf{E} = \frac{1}{2} [\nabla \mathbf{u} + \nabla \mathbf{u}^T]$.

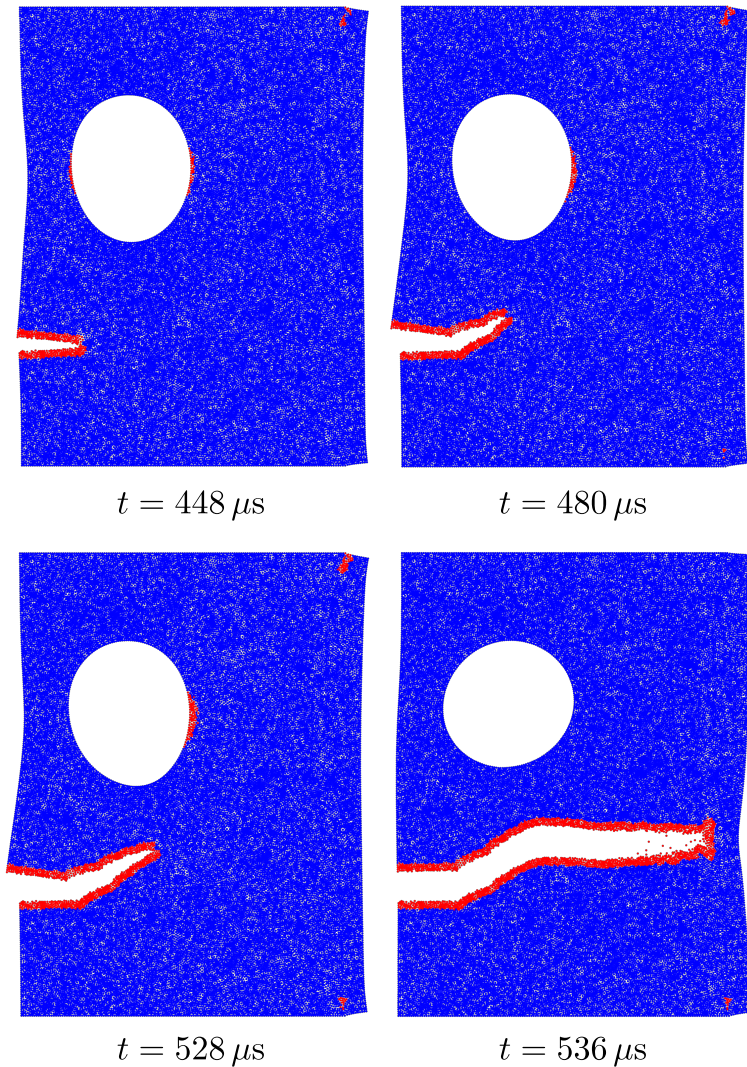


Figure 21: **Circular hole and pre-crack problem:** Plot of damage in the deformed configuration after scaling the displacement field by 50 to show the crack opening.

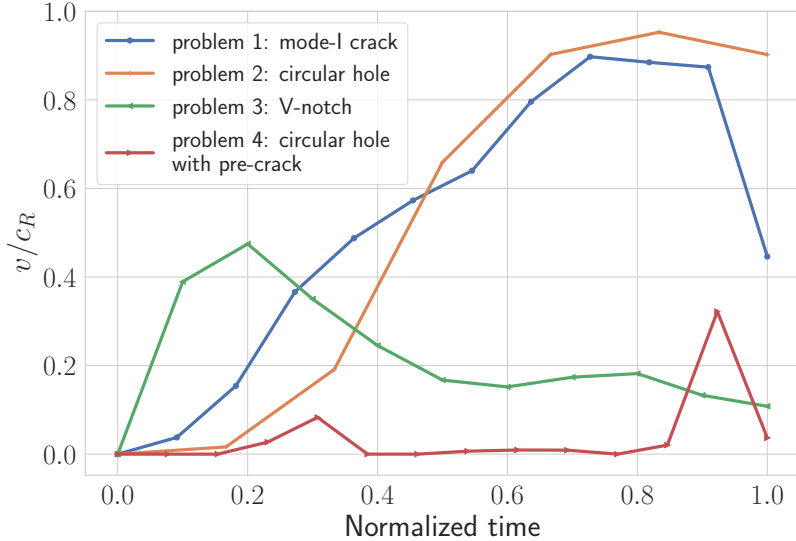


Figure 22: Comparison of the normalized crack speed for the four problems.

8. Conclusion

This work analyzed the nodal finite element approximation for the peridynamics. Assuming exact solutions are in proper function spaces, consistency errors are shown to be bounded, and a-priori convergence of the discretization is established. The nodal finite element discretization implementation is discussed in detail, and a range of numerical experiments are performed using the method to show the utility of the approximation. The nodal finite element approximation is relatively straightforward and can be easily integrated with the standard finite element meshing libraries. Further, the method is computationally faster than the standard finite element approximation because the mass matrix is diagonal, and the nonlocal force calculation is similar to finite-difference/mesh-free approximation. Since NFEA is based on finite element representation and mesh, the coupling peridynamics with other PDE-based models for multiphysics simulation is straightforward.

The work also presents an alternative NFEA method based on Clément interpolation. This work considers Clément interpolation only theoretically. The a-priori error estimates in the alternative NFEA improve the NFEA a-priori error estimates, and the regularity requirement on the exact solution in Clément NFEA is less restrictive. Future work will explore implementing the alternative NFEA method and developing a-posteriori error estimates.

Acknowledgements

The majority of the work is done through the support of the U.S. Army Research Laboratory and the U.S. Army Research Office under contract/grant number W911NF1610456 RL. PKJ is also thankful to the Oden Institute for Computational Engineering and Sciences, The University of Texas at Austin, for providing resources to run some simulations. PD is thankful to the LSU Center of Computation & Technology for supporting this work.

References

- Agwai, A., Guven, I., and Madenci, E. (2011). Predicting crack propagation with peridynamics: a comparative study. *International journal of fracture*, 171(1):65–78. [1](#)

- Ahrens, J., Geveci, B., and Law, C. (2005). Paraview: An end-user tool for large data visualization. *The visualization handbook*, 717. [7](#)
- Aksoylu, B. and Unlu, Z. (2014). Conditioning analysis of nonlocal integral operators in fractional sobolev spaces. *SIAM Journal on Numerical Analysis*, 52:653–677. [1](#)
- Ambrosio, L. and Brades, A. (1997). *Energies in SBV and variational models in fracture mechanics: Homogenization and Applications to Materials Science*, volume 9. Gakuto, Gakkotosho, Tokyo, Japan. [1](#)
- Ambrosio, L., Coscia, A., and Dal Maso, G. (1997). Fine properties of functions with bounded deformation. *Archive for Rational Mechanics and Analysis*, 139(3):201–238. [1](#)
- Anicode, S. V. K. and Madenci, E. (2022). Bond-and state-based peridynamic analysis in a commercial finite element framework with native elements. *Computer Methods in Applied Mechanics and Engineering*, 398:115208. [1](#)
- Bobaru, F. and Hu, W. (2012). The meaning, selection, and use of the peridynamic horizon and its relation to crack branching in brittle materials. *International journal of fracture*, 176(2):215–222. [1](#), [2](#)
- Brenner, S. and Scott, R. (2007). *The mathematical theory of finite element methods*, volume 15. Springer Science & Business Media, 3 edition. [3](#)
- Chen, X. and Gunzburger, M. (2011). Continuous and discontinuous finite element methods for a peridynamics model of mechanics. *Computer Methods in Applied Mechanics and Engineering*, 200(9-12):1237–1250. [1](#)
- Clément, P. (1975). Approximation by finite element functions using local regularization. *RARO Anal. Numér.*, 9:77–84. [3](#)
- Dai, S., Augarde, C., Du, C., and Chen, D. (2015). A fully automatic polygon scaled boundary finite element method for modelling crack propagation. *Engineering Fracture Mechanics*, 133:163–178. [7](#), [7.7](#)
- De Meo, D. and Oterkus, E. (2017). Finite element implementation of a peridynamic pitting corrosion damage model. *Ocean Engineering*, 135:76–83. [1](#)
- Diehl, P., Jha, P. K., Kaiser, H., Lipton, R., and Lévesque, M. (2020). An asynchronous and task-based implementation of peridynamics utilizing hpx—the c++ standard library for parallelism and concurrency. *SN Applied Sciences*, 2(12):1–21. [7](#)
- Diehl, P., Prudhomme, S., and Lévesque, M. (2019). A review of benchmark experiments for the validation of peridynamics models. *Journal of Peridynamics and Nonlocal Modeling*, 1:14–35. [1](#)
- Diyaroglu, C., Oterkus, S., Oterkus, E., and Madenci, E. (2017). Peridynamic modeling of diffusion by using finite-element analysis. *IEEE Transactions on Components, Packaging and Manufacturing Technology*, 7(11):1823–1831. [1](#)
- Du, Q., Tao, Y., and Tian, X. (2018). A peridynamic model of fracture mechanics with bond-breaking. *Journal of Elasticity*, 132(2):197–218. [1](#)
- Emmrich, E., Lehoucq, R. B., and Puhst, D. (2013). Peridynamics: a nonlocal continuum theory. In *Meshfree Methods for Partial Differential Equations VI*, pages 45–65. Springer. [1](#)
- Foster, J. T., Silling, S. A., and Chen, W. (2011). An energy based failure criterion for use with peridynamic states. *International Journal for Multiscale Computational Engineering*, 9(6). [1](#)
- Geuzaine, C. and Remacle, J.-F. (2009). Gmsh: A 3-d finite element mesh generator with built-in pre-and post-processing facilities. *International journal for numerical methods in engineering*, 79(11):1309–1331. [7](#)
- Ghajari, M., Iannucci, L., and Curtis, P. (2014). A peridynamic material model for the analysis of dynamic crack propagation in orthotropic media. *Computer Methods in Applied Mechanics and Engineering*, 276:431–452. [1](#)
- Ha, Y. D. and Bobaru, F. (2010). Studies of dynamic crack propagation and crack branching with peridynamics. *International Journal of Fracture*, 162(1-2):229–244. [1](#)
- Huang, X., Bie, Z., Wang, L., Jin, Y., Liu, X., Su, G., and He, X. (2019). Finite element method of bond-based peridynamics and its abaqus implementation. *Engineering Fracture Mechanics*, 206:408–426. [1](#)
- Jha, P. and Lipton, R. (2021). Finite element approximation of nonlocal dynamic fracture models. *Discrete & Continuous Dynamical Systems-B*, 26(3):1675. [1](#), [2.1](#), [3.2](#), [4](#), [4.1](#), [4.1](#), [4.2](#), [5](#)
- Jha, P. K., Desai, P. S., Bhattacharya, D., and Lipton, R. (2021). Peridynamics-based discrete element method (peridem) model of granular systems involving breakage of arbitrarily shaped particles. *Journal of the Mechanics and Physics of Solids*, 151:104376. [1](#)
- Jha, P. K. and Diehl, P. (2021). Nlmech: Implementation of finite difference/meshfree discretization of nonlocal fracture models. *Journal of Open Source Software*, 6(65):3020. [7](#)
- Jha, P. K. and Lipton, R. (2018a). Numerical analysis of nonlocal fracture models in holder space. *SIAM Journal on Numerical Analysis*, 56(2):906–941. [1](#), [6](#)
- Jha, P. K. and Lipton, R. (2018b). Numerical convergence of nonlinear nonlocal continuum models to local elastodynamics. *International Journal for Numerical Methods in Engineering*, 114(13):1389–1410. [1](#)
- Jha, P. K. and Lipton, R. (2019). Numerical convergence of finite difference approximations for state based peridynamic fracture models. *Computer Methods in Applied Mechanics and Engineering*, 351:184–225. [1](#), [7](#), [7.4.1](#)
- Jha, P. K. and Lipton, R. (2020a). Finite element convergence for state-based peridynamic fracture models. *Communications on Applied Mathematics and Computation*, 2(1):93–128. [1](#)
- Jha, P. K. and Lipton, R. P. (2020b). Kinetic relations and local energy balance for lefm from a nonlocal peridynamic model. *International Journal of Fracture*. [1](#)
- Lipton, R. (2014). Dynamic brittle fracture as a small horizon limit of peridynamics. *Journal of Elasticity*, 117(1):21–50. [1](#), [2](#)
- Lipton, R. (2016). Cohesive dynamics and brittle fracture. *Journal of Elasticity*, 124(2):143–191. [1](#), [2](#), [2](#), [6](#), [6](#), [6](#), [7.2](#)
- Lipton, R., Silling, S., and Lehoucq, R. (2016). Complex fracture nucleation and evolution with nonlocal elastodynamics. *arXiv preprint arXiv:1602.00247*. [1](#)
- Lipton, R. P., Lehoucq, R. B., and Jha, P. K. (2019). Complex fracture nucleation and evolution with nonlocal elastodynamics. *Journal of Peridynamics and Nonlocal Modeling*, 1(2):122–130. [1](#), [7](#), [7.4.1](#)

- Liu, W. and Hong, J.-W. (2012). A coupling approach of discretized peridynamics with finite element method. *Computer methods in applied mechanics and engineering*, 245:163–175. [1](#)
- Macek, R. W. and Silling, S. A. (2007). Peridynamics via finite element analysis. *Finite Elements in Analysis and Design*, 43(15):1169–1178. [1](#)
- Madenci, E., Dorduncu, M., Barut, A., and Phan, N. (2018). A state-based peridynamic analysis in a finite element framework. *Engineering Fracture Mechanics*, 195:104–128. [1](#)
- Mengesha, T. and Du, Q. (2015). On the variational limit of a class of nonlocal functionals related to peridynamics. *Nonlinearity*, 28(11):3999. [1](#)
- Ni, T., Zhu, Q.-z., Zhao, L.-Y., and Li, P.-F. (2018). Peridynamic simulation of fracture in quasi brittle solids using irregular finite element mesh. *Engineering Fracture Mechanics*, 188:320–343. [1](#)
- Royer, D. and Clorennec, D. (2007). An improved approximation for the rayleigh wave equation. *Ultrasonics*, 46(1):23–24. [7.2](#)
- Seleson, P., Du, Q., and Parks, M. L. (2016). On the consistency between nearest-neighbor peridynamic discretizations and discretized classical elasticity models. *Computer Methods in Applied Mechanics and Engineering*, 311:698–722. [1](#)
- Shojaei, A., Zaccariotto, M., and Galvanetto, U. (2017). Coupling of 2d discretized peridynamics with a meshless method based on classical elasticity using switching of nodal behaviour. *Engineering Computations*, 34(5):1334–1366. [1](#)
- Silling, S. (2003). Dynamic fracture modeling with a meshfree peridynamic code. In *Computational fluid and solid mechanics 2003*, pages 641–644. Elsevier. [1](#)
- Silling, S., Weckner, O., Askari, E., and Bobaru, F. (2010). Crack nucleation in a peridynamic solid. *International Journal of Fracture*, 162(1-2):219–227. [1](#)
- Silling, S. A. (2000). Reformulation of elasticity theory for discontinuities and long-range forces. *Journal of the Mechanics and Physics of Solids*, 48(1):175–209. [1, 2](#)
- Silling, S. A. and Askari, E. (2005). A meshfree method based on the peridynamic model of solid mechanics. *Computers & structures*, 83(17):1526–1535. [1, 7, 7.4.1](#)
- Silling, S. A. and Bobaru, F. (2005). Peridynamic modeling of membranes and fibers. *International Journal of Non-Linear Mechanics*, 40(2):395–409. [1](#)
- Silling, S. A., Epton, M., Weckner, O., Xu, J., and Askari, E. (2007). Peridynamic states and constitutive modeling. *Journal of Elasticity*, 88(2):151–184. [1](#)
- Silling, S. A. and Lehoucq, R. B. (2008). Convergence of peridynamics to classical elasticity theory. *Journal of Elasticity*, 93(1):13–37. [1](#)
- Silling, S. A. and Lehoucq, R. B. (2010). Peridynamic theory of solid mechanics. *Advances in applied mechanics*, 44:73–168. [1](#)
- Trageser, J. and Seleson, P. (2020). Bond-based peridynamics: A tale of two poisson's ratios. *Journal of Peridynamics and Nonlocal Modeling*, 2(3):278–288. [7.2](#)
- Trask, N., You, H., Yu, Y., and Parks, M. L. (2019). An asymptotically compatible meshfree quadrature rule for nonlocal problems with applications to peridynamics. *Computer Methods in Applied Mechanics and Engineering*, 343:151–165. [1](#)
- Weckner, O. and Abeyaratne, R. (2005). The effect of long-range forces on the dynamics of a bar. *Journal of the Mechanics and Physics of Solids*, 53(3):705–728. [1](#)
- Wildman, R. A., O'Grady, J. T., and Gazonas, G. A. (2017). A hybrid multiscale finite element/peridynamics method. *International Journal of Fracture*, 207(1):41–53. [1](#)
- Yang, Z., Oterkus, E., Nguyen, C. T., and Oterkus, S. (2019). Implementation of peridynamic beam and plate formulations in finite element framework. *Continuum Mechanics and Thermodynamics*, 31:301–315. [1](#)